remote sensing

MDPI

Article

Satellite-Based Thermophysical Analysis of Volcaniclastic Deposits: A Terrestrial Analog for Mantled Lava Flows on Mars

Mark A. Price [1,*], Michael S. Ramsey [1] and David A. Crown [2]

[1] Department of Geology and Planetary Science, University of Pittsburgh, 4107 O'Hara Street, Pittsburgh, PA 15260, USA; mramsey@pitt.edu

[2] Planetary Science Institute, 1700 East Ft. Lowell Rd., Suite 106, Tucson, AZ 85719, USA; crown@psi.edu

* Correspondence: markprice88@gmail.com; Tel.: +1-412-624-8780; Fax: +1-412-624-3914

Academic Editors: Richard Gloaguen and Prasad S. Thenkabail

Received: 7 October 2015; Accepted: 25 January 2016; Published: 17 February 2016

Abstract: Orbital thermal infrared (TIR) remote sensing is an important tool for characterizing geologic surfaces on Earth and Mars. However, deposition of material from volcanic or eolian activity results in bedrock surfaces becoming significantly mantled over time, hindering the accuracy of TIR compositional analysis. Moreover, interplay between particle size, albedo, composition and surface roughness add complexity to these interpretations. Apparent Thermal Inertia (ATI) is the measure of the resistance to temperature change and has been used to determine parameters such as grain/block size, density/mantling, and the presence of subsurface soil moisture/ice. Our objective is to document the quantitative relationship between ATI derived from orbital visible/near infrared (VNIR) and thermal infrared (TIR) data and tephra fall mantling of the Mono Craters and Domes (MCD) in California, which were chosen as an analog for partially mantled flows observed at Arsia Mons volcano on Mars. The ATI data were created from two images collected ~12 h apart by the Advanced Spaceborne Thermal Emission and Reflection Radiometer (ASTER) instrument. The results were validated with a quantitative framework developed using fieldwork that was conducted at 13 pre-chosen sites. These sites ranged in grain size from ash-sized to meter-scale blocks and were all rhyolitic in composition. Block size and mantling were directly correlated with ATI. Areas with ATI under 2.3×10^{-2} were well-mantled with average grain size below 4 cm; whereas values greater than 3.0×10^{-2} corresponded to mantle-free surfaces. Correlation was less accurate where checkerboard-style mixing between mantled and non-mantled surfaces occurred below the pixel scale as well as in locations where strong shadowing occurred. However, the results validate that the approach is viable for a large majority of mantled surfaces on Earth and Mars. This is relevant for determining the volcanic history of Mars, for example. Accurate identification of non-mantled lava surfaces within an apparently well-mantled flow field on either planet provides locations to extract important mineralogical constraints on the individual flows using TIR data.

Keywords: Apparent Thermal Inertia (ATI); ASTER; volcanic terrain; Mono Craters; Arsia Mons; Mars

1. Introduction

The erosion, transport and deposition of fine-grained particulates over bedrock surfaces serve as indicators of the past and more recent volcanic and eolian processes on Earth and Mars. For example, lava flows and other recently emplaced volcanic terrains on the Earth commonly become covered by remobilized ash, tephra fall and/or material from pyroclastic density currents (PDC's). In comparison, the movement of sand and dust over time on the surface of Mars significantly modifies

the exposure of any bedrock surfaces [1]. Identification of the major rock-forming minerals that comprise the underlying rocks is important to understand the geologic and petrologic history of the planet and is possible with thermal infrared (TIR) remote sensing data [2–4]. However, the pervasive mantling typically masks these spectral signatures with the relatively featureless TIR spectrum of the fine-grained material [5–7]. Therefore, the higher albedo regions (e.g., regions with more dust mantling) on Mars are generally avoided during TIR spectral analyses.

Similarly, surfaces on Earth mantled to any degree must be treated cautiously during TIR spectral analysis. Fine-grained mantling of bedrock exposures on Earth is not as pervasive as on Mars due mainly to the higher rates of weathering. Consistent erosion on shorter time scales (e.g., years to centuries) and tectonic processes over much longer time scales (e.g., millions of years) remove this material. However, mantling is found on younger surfaces and/or those that experience higher rates of new mantling due to a variety of processes (e.g., explosive volcanic eruptions, eolian deposition, and desertification). Knowledge of the presence of these mantling deposits and, perhaps more importantly, identification of their composition and that of the underlying rocks, becomes invaluable in active volcanic environments, for example. Mantling in these locations may arise from a recent eruption, with the direction and thickness of the tephra fall deposits indicating the magnitude of the eruption and wind direction at the time, whereas the composition of the pyroclastic material reveals information about any evolution of the eruption or magmatic center over time. Analysis of the composition of active dunes can also relay similar information about the underlying substrate as well as the paleo-environmental conditions that produced the dunes [8–10].

Some regions of Mars have become heavily mantled by deposits that were derived locally, and thus retain the chemical and spectral signatures of the underlying rocks [11,12]. More generally, however, fine-grained surface materials have become globally-homogenized and therefore hinder accurate characterization of the underlying bedrock from orbit [13,14]. This mantling is observed to be spatially variable in areas such as the lava flow fields south of Arsia Mons. This field contains flows that are visibly similar and in close proximity but have very different thermophysical properties (Figure 1). This region was examined in prior studies and shown to contain some of the roughest terrain on Mars with flows that are geologically young (~100 My) for Mars [4,15–19].

The Arsia flows display unusual thermophysical properties such as variable and distinct diurnal temperature changes that vary from flow to flow and even within a given flow. This behavior motivated the objective of the current study, which is to assess the applicability of using a thermophysical analysis approach to determine the presence and degree of mantling on these flows by first validating it on an Earth analog site. Although deriving information from mantled surfaces using TIR data is difficult, orbital thermophysical measurements have been used to approximate the thickness of such deposits overlying bedrock layers on Mars and Earth [9,10,20]. Furthermore, locating specific bedrock regions within mantled flows that either protrude through the fine-grained covering or are only thinly-mantled is one possible approach that could be used to determine the composition of those regions [4,17,18].

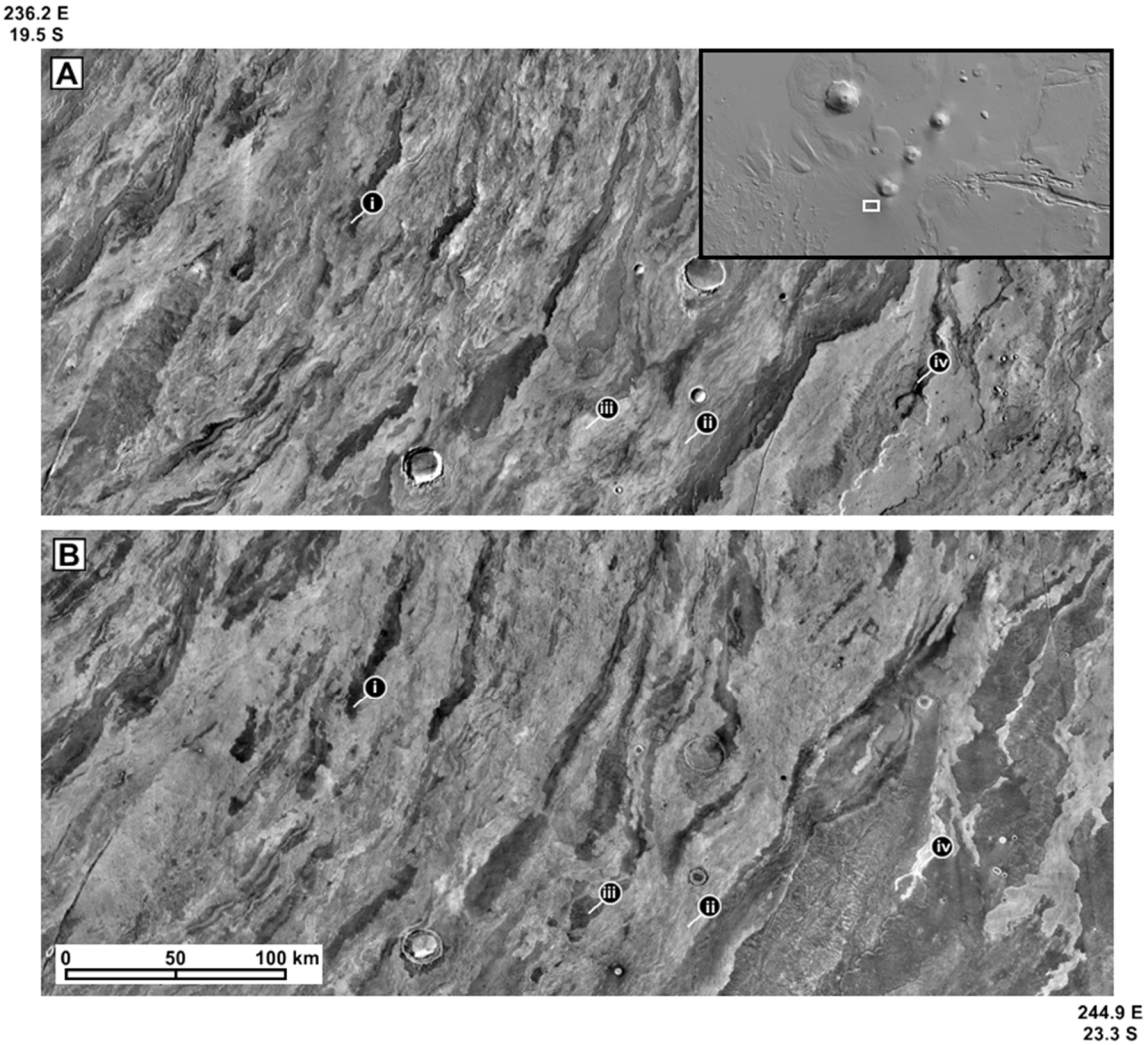

Figure 1. THEMIS IR global composite (100 pixel/degree) of a portion of the southern Arsia Mons flow field. (**A**) Day; (**B**) Night. Locator pins identify common examples of the four different thermophysical behaviors exhibited by individual lava flows over the diurnal cycle: (i) unchanging temperature, always cool; (ii) unchanging temperature, always warm; (iii) changing temperature; warm during the day and cool at night, indicative of a low thermal inertia surface; (iv) changing temperature, cool during the day and warm at night, indicative of a high thermal inertia surface. Inset is a MOLA-derived shaded relief image with the study area denoted by the white box.

The Mono Craters and Domes (MCD) in east-central California were chosen because many of the obsidian-rich, rhyolitic composition lava flows are mantled by material with much finer grain sizes (Figure 2). Although not a direct compositional analog for Mars, the mantled flows and domes of the MCD provide an excellent process and technique analog [14,21–23]. The rough, blocky flows and domes display a wide range of tephra mantling depth on their surfaces, from heavily mantled (e.g., >10 cm) by tephra to areas that are non-mantled. These surfaces span many dozens of TIR 90 m scale pixels or can be within meters of each other, therefore providing all scales of spatial mixing and mantling depths. The similar albedo and composition of the lava flows to the mantling deposits hinders discrimination using purely spectral data such as VNIR reflectance or TIR emissivity. This is analogous to the case on Mars, however with mainly basaltic compositions. Furthermore, the ability to validate the satellite data using ground and laboratory data (Figure 3) provides the opportunity to test the accuracy of using a thermophysical rather than a spectral approach. This study uses spaceborne-derived data to first identify the mantled regions on domes of the MCD followed by field

validation of those regions and later quantification of field samples using laboratory spectral and petrographic techniques. This tiered approach allows the image data to guide the field mapping and the field and laboratory data to later quantify the initial results from image analysis, thus producing a particle/block size map from the ATI data.

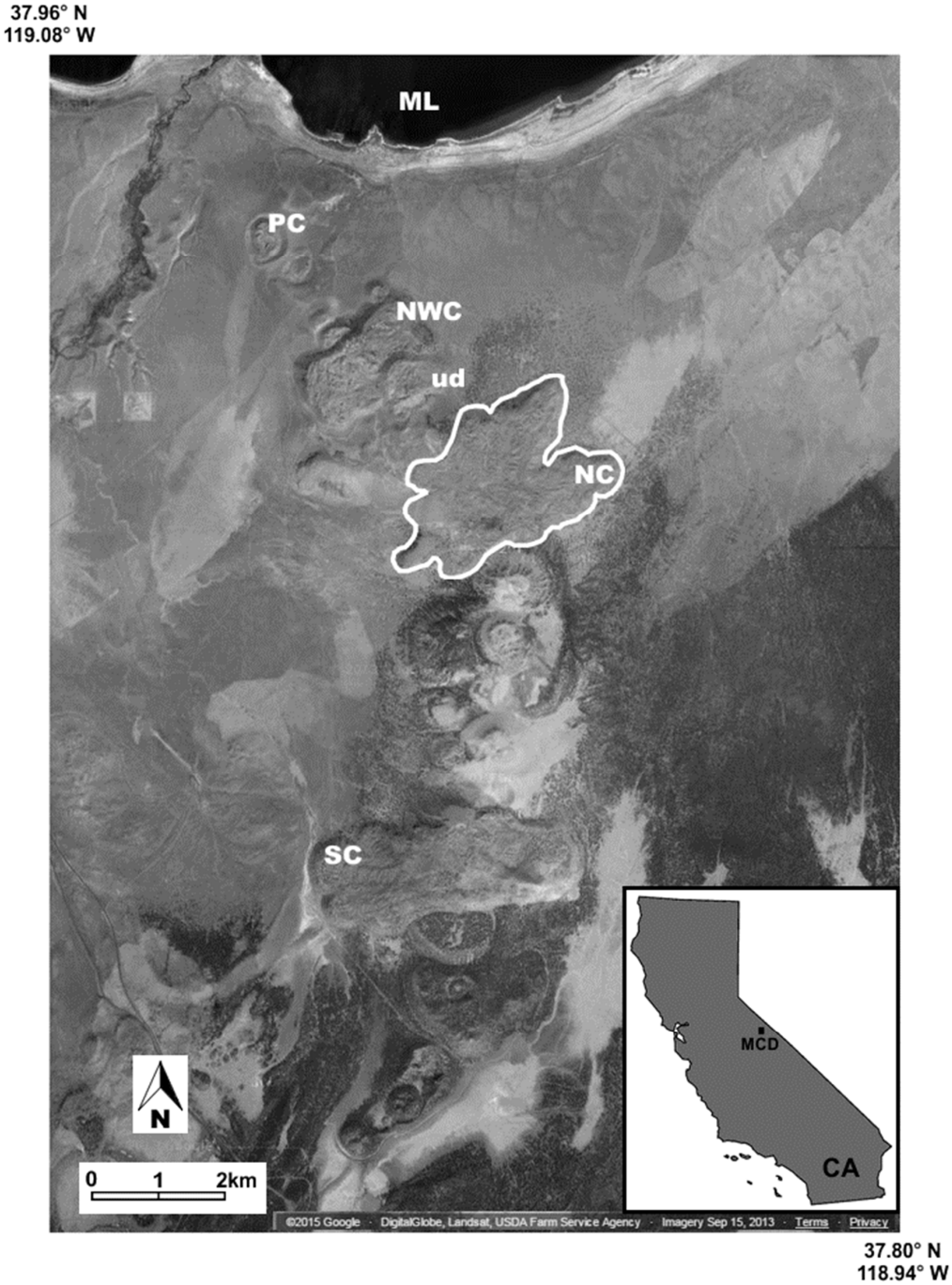

Figure 2. High-resolution visible satellite image from Digital Globe (within Google Earth) the Mono Craters and Domes with North Coulee (NC) outlined in white. Other features include: Mono Lake (ML), Panum Crater (PC), Northwest Coulee (NWC), South Coulee (SC), and the informally-named Upper Dome (UD). Inset shows the state of California with the study area (MCD) denoted by the black box.

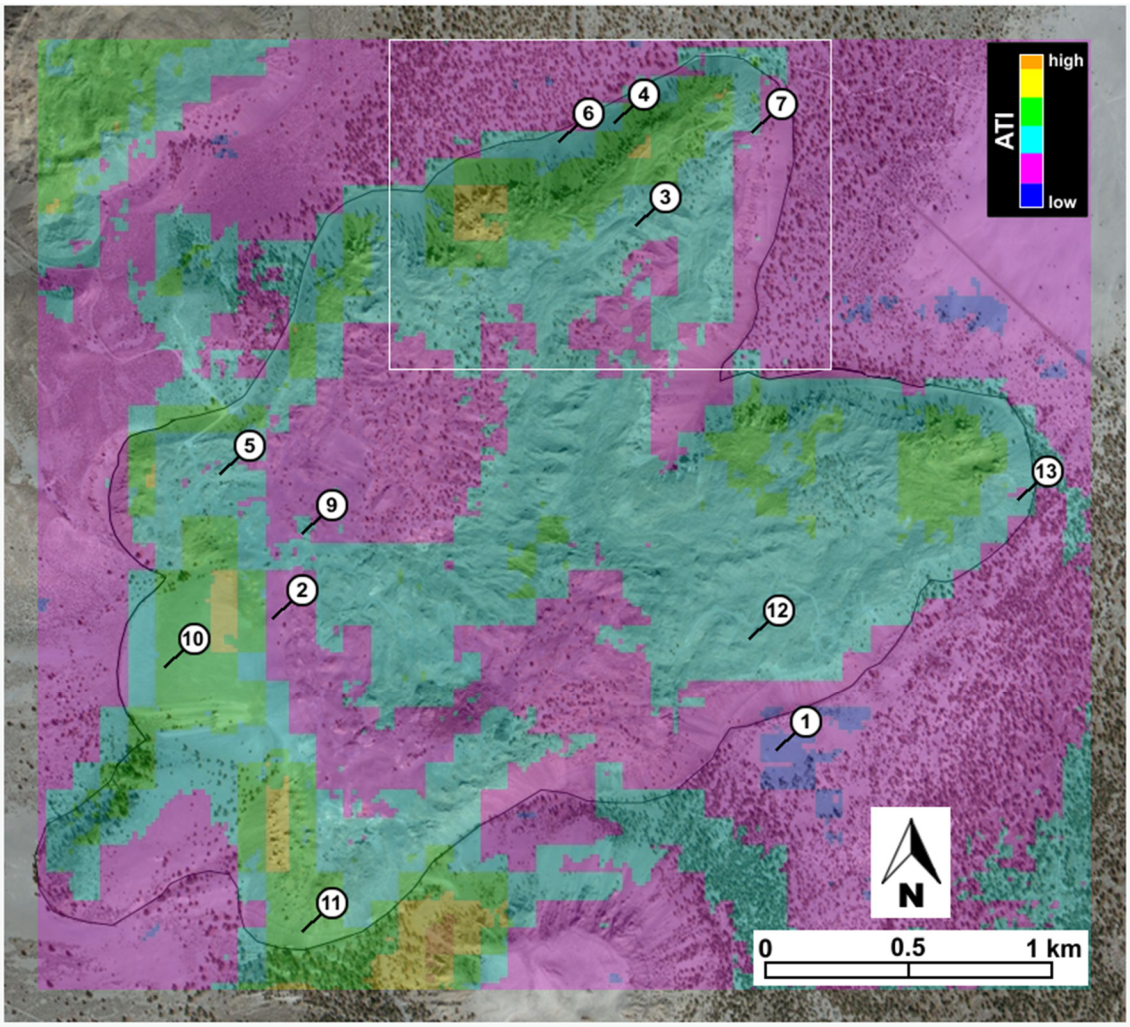

Figure 3. Relative apparent thermal inertia image of North Coulee (outlined in black) derived from 10 July 2011 ASTER data (created by Ramsey and Crown, 2010) [4]. The colorized scale image is overlain on a Digital Globe (within Google Earth) high-resolution color image for detail. This image was used as a guide for later fieldwork and the numbered pins refer to visited field sites. The white box denotes the area shown in Figure 6. Data courtesy of NASA/GSFC/METI/Japan Space Systems. U.S./Japan ASTER Science Team.

2. Background

2.1. Terrestrial TIR Data

The Advanced Spaceborne Thermal Emission and Reflection Radiometer (ASTER) instrument is one of five on the Terra platform [24] and has acquired data since its launch in December 1999. ASTER data have improved local- and regional-scale understanding of various processes, including surface-atmosphere interactions, geology, and volcanic activity [25]. ASTER has three spectral channels in the VNIR wavelength region, six in the shortwave infrared (SWIR) wavelength region, and five in the TIR wavelength region, with resolutions of 15 m/pixel, 30 m/pixel, and 90 m/pixel, respectively [25]. The SWIR data are no longer acquired, however, due to a failed detector cooling system. The spectral range and moderately high spatial resolution of the VNIR and TIR allow a variety of surface materials to be distinguished and a better understanding of compositional mixing within a given pixel or region of pixels [10,25].

2.2. Mars Thermophysical Data

Thermal Inertia (TI) is an important remote sensing tool for identifying certain physical properties of a surface such as the particle size, cementation state, and/or soil moisture content [9,26,27]. It can be thought of as a measure of the resistance of a surface material to temperature change over some time scale [28] and is defined as

$$TI = (K\rho c)^{1/2} \quad (1)$$

where K is the thermal conductivity ($W \cdot m^{-1} \cdot K^{-1}$), ρ is the density ($kg \cdot m^{-3}$), and c is the specific heat ($J \cdot kg^{-1} \cdot K^{-1}$) giving TI units of $J \cdot m^{-2} \cdot K^{-1} \cdot s^{-1/2}$. TI nor the terms that comprise it can be determined directly from satellite measurements and therefore it must either be approximated or modeled where only remote sensing is available.

The relative simplicity of the Martian atmosphere and surface compared to Earth has allowed well-described thermal models to be developed, which predict the surface temperature at any time during the day in different seasons and various latitudes [29–31]. Modeled diurnal temperature curves are then fit to measurements of two or more temperatures from orbital instruments and used to estimate physical parameters that influence TI such as the presence and amount of bedrock and blocks on the surface, particle size of the sediments, layering, *etc.* For example, Kieffer *et al.* (1977) [32] and Palluconi and Kieffer (1981) [29] use this approach to differentiate between different surface types on the planet. Edgett and Christensen (1991) [33] expand on the work of Christensen (1982) [34] to determine the particle size of unconsolidated materials in Martian dunes. Mellon *et al.* (2000) [35] compare thermal inertia to thermal emission spectrometer (TES) observations of the Martian surface to determine the small-scale variability on the planet's surface by mapping particle size, rock abundance, and exposures of bedrock. Christensen *et al.* (2001) [2] apply TES-derived thermal inertia to interpret the composition of Martian surface materials, rocks, ices, and the thermal properties of the surface. Putzig *et al.* (2005) [36] create a new thermal inertia map of Mars and use it to quantify new surface units of low and high thermal inertia. The work of Rogers *et al.* (2005) [37] use Thermal Emission Imaging System (THEMIS) multispectral and thermophysical data combined with TES hyperspectral and albedo readings to determine the mineralogical heterogeneity of Martian bedrock exposed at Ares Valles. Edwards *et al.* (2009) [38] expand upon that work to identify numerous other bedrock outcrops on Mars using thermal inertia.

2.3. Apparent Thermal Inertia

Similar quantitative thermophysical modeling for Earth surfaces is typically much more difficult with complications that include (but are not limited to) the effects of soil moisture, especially if there is a change between the day and night data collection; atmospheric thickness, condensation and gas conductivity, all of which make modeling of the grain to grain heat transfer more complex. Earth's thick heterogeneous atmosphere absorbs and scatters energy in the visible to thermal infrared wavelength regions. Additionally, it hinders the efficiency of radiant transfer of energy between the grains of a particulate surface. Diurnal temperature variations are also more sensitive to atmospheric humidity and precipitation, which reduces the accuracy of thermal inertia estimates [39–42]. Thermal inertia investigations of Earth must also account for vegetative cover, which obscures geologic surfaces in addition to effecting albedo and surface temperature. Despite these factors, thermal inertia has been used successfully on Earth, most commonly to map the moisture content of soils and for geologic interpretations [9,39–42]. Cracknell and Xue (1996) [43] use data from the Advanced Very High Resolution Radiometer (AVHRR) sensor to create thermal inertia images to estimate surface heat flux after consulting local weather data. A study by Sobrino and El Kharraz (1999a) [44] expands on this work by successfully applying a derived thermal inertia proxy to AVHRR images of a region of Niger. Additional maps were created of the Iberian Peninsula and Morocco [45]. More recently, Scheidt *et al.* (2010) [9] use ASTER-derived thermophysical data to create high-spatial resolution soil moisture maps

of the White Sands dune field in New Mexico and successfully identify an extreme drying period that later led to a large-scale dust emission event from the region.

The complexity of thermal inertia modeling on Earth has led to the creation of Apparent Thermal Inertia (ATI) as a proxy. In the terrestrial literature, ATI is commonly referred to the semi-quantitative approximation for the actual thermophysical response (*i.e.*, thermal inertia) using data from the VNIR, SWIR and TIR regions. It is defined as:

$$ATI = (1 - a)/(\Delta T) \quad (2)$$

where a is the broadband VNIR/SWIR albedo and ΔT is the temperature difference between a day and night pair of coregistered TIR images. Therefore, ATI is a unitless measure of the reflected solar albedo relative to the difference in emitted brightness temperature over the diurnal cycle [9,28,46,47].

The use of apparent thermal inertia in the Martian literature is quite different [9,46,48]. In past studies, ATI simply denotes apparent seasonal or yearly differences in thermal inertia for the same surface. For example, Putzig and Mellon (2007) [48] investigate surface heterogeneity and the effects of diurnal and seasonal change on thermal inertia models, calling these differences "apparent" thermal inertia. In this study, we use the traditional semi-quantitative terrestrial definition of ATI.

2.4. The Mono Craters and Domes

The MCD, 25–30 km north of the town of Mammoth Lakes, California, is an arcuate chain of craters and high-silica lava flows (Figure 2). The most recent phase of activity occurred over the past 10,000 years and therefore represents some of the youngest activity in the Long Valley Caldera region [49]. The chain consists of an alignment of approximately 28 domes, craters, and coulees. The coulees have relief greater than 600 m above the surrounding terrain and a maximum elevation of 2800 m [50]. The vents also have associated tephra rings and extensive aprons of pumiceous fall, flow, and reworked deposits [49–51]. Beginning in the Holocene, the Mono system spread both north and south from the current central part of the dome chain, producing dike-fed domes of crystal-poor, high-silica rhyolite [49]. A volumetric eruption rate of ~0.2 km^3/ka in the early Holocene increased to about 0.8 km^3/ka during the last 3000 years [52]. This volumetric surge coincided with a switch from crystal-poor to virtually aphyric rhyolite [52,53]. Composition of the MCD lavas is similar for all younger effusive deposits in the region. All lavas but one (an undated crystal-rich rhyodacite at 68 wt.% SiO_2) at the Mono Craters is high-silica (75.4 wt.%–77 wt.% SiO_2) rhyolite [49]. Major element (and most trace-element) contents are quite similar to those of Glass Mountain and the early Bishop Tuff [49].

The youngest eruptions in the MCD chain date to approximately the fourteenth century [49,54,55]. These eruptions produced 0.2 km^3 of pyroclastic fall, flow, and surge deposits and 0.4 to 1.0 km^3 of lava domes and flows [53,54]. These rhyolitic lavas originated from five aligned vents in the northwestern zone of the Mono chain. According to Bailey (1989) [53], the modern exposures at Northwestern Coulee, Panum Crater, Upper Dome, Crater Dome, and North Coulee were all directly formed during this eruptive phase (Figure 2). Eruption sequences generally consisted of explosive sub-Plinian events that formed thick deposits of tephra fall on older domes within a few kilometers of the vent followed by pyroclastic flows and surges and finally extrusion of the viscous dome-forming lavas [53,54].

2.5. The Arsia Mons Flow Field

Arsia Mons, the southernmost of the three prominent Tharsis shield volcanoes, has a well-developed summit caldera and extensive lava flow fields [56–60]. There are two large flow aprons with a multitude of individual flows and flow lobes that extend from alcoves on the lower NE and SW flanks of the volcano, which postdate its main shield [22,23,61,62]. Previous work in the area includes series of 1:2M scale lava flow maps of the Tharsis region by Scott (1981) [63] and Scott *et al.* (1981a,b) [64,65] using Viking Orbiter images. More recent studies use Mars Express High Resolution

Stereo Camera (HRSC) images to examine stages in effusive volcanism in the Tharsis region, including the Arsia Mons shield [66,67]. Lang *et al.* (2009) [23] examine this flow field further south and found it to be basaltic with a possible affinity to the basaltic shergottites class of SNC meteorites.

Like the Mono Craters, the Tharsis region has been imaged by high-resolution VNIR and TIR datasets and is shown to contain aerially extensive lava flow fields with variable amounts of mantling derived from both eolian infilling of the flow surfaces and airfall dust. These flows have a Thermal Emission Spectrometer (TES) derived albedo of between 0.22 and 0.24 and a dust cover index of between 0.95 and 0.97 [14,62], which generally denotes a less than desirable, region for thermal infrared spectral analyses due to the presence of dust.

3. Methodology

This investigation is designed to validate the assumption that thermophysical variability is directly related to the degree of mantling and its particle size on volcanic surfaces through the combined use of image, field, and laboratory data. Therefore, it serves as a terrestrial analog calibration/validation study to ongoing thermal inertia studies of the mantled flow fields on Mars.

A preliminary study by Ramsey and Crown (2010) [4,19] noted statistically significant variations in ATI for the MCD chain (Figure 3). However, the qualitative study merely showed that ATI did correlate to the mantled regions of the MCD shown in high-resolution visible images. Therefore, the methodological approach used here was to recreate the results of Ramsey and Crown (2010) [4] and then develop a more quantitative validation of the ATI product. New ATI images were created showing pixel-by-pixel difference in ATI as compared to the regional differences seen in the 2010 study. These data were compared with high-resolution visible satellite images, and then used to preselect field site locations. These field sites represent the full range of ATI values, mantled and unmantled surfaces as well as those at different elevations and slopes. Data were acquired at 13 field sites including samples collected for later laboratory analysis. Analysis of the field and laboratory results allow quantitative constraints to be placed on the ATI results, including extrapolating to larger block sizes than would normally not be resolved by ATI alone.

After an extensive examination of the various flows within the MCD, North Coulee was chosen as the field study site. It is one of the largest (~0.4 km^3) of the recent lava flows, comprising over half the total volume of all the fourteenth century eruptions [54,68]. The coulee contains a wide variety of mantled surfaces that have identical composition to the volcanic flows found in the area. These mantled surfaces originated from the deposition of tephra produced during younger eruptions to the north.

Prior studies showed that the calculation of ATI provides a reasonable proxy for identification of the mantled zones on the domes [17,18,62]. For this study, four ASTER image pairs of the Mono Craters spanning several years were chosen and ATI was calculated for each. Cloud free, chronologically-similar (within 12–30 h of each other) day and night level 1B ASTER images were first identified. The day and night images were as close in time to one another as possible considering the latitude, acquisition, and geometry limitations of the ASTER instrument. The data pair from July 2011 was chosen because the day and night images were obtained less than 12 h apart and the weather conditions were ideal. Average relative humidity on 10 July 2011 (day of the ASTER overpasses used for this work) was 33% (Table 1) (Weather Underground, 2013). Precipitation records from Sonora Junction, CA (~60 km from MCD) and Bridgeport, CA (~45 km from MCD) were used to verify that there were no large rain events either before or within the image pair acquisition that could affect the ATI results. Records from these stations indicate a scarcity in precipitation in the month prior to the ASTER overpass and none during the overpass interval [69]. Furthermore, the low humidity, high surface porosity, and an average temperature in July of ~29 °C [69,70] minimizes the possibility of any surface moisture.

Table 1. Precipitation records for the closest weather stations to the Mono Craters (Sonora Junction, CA and Bridgeport, CA). Note the lack of rain before the ASTER overflights (10 July 2011) from which the ATI data are based.

Bridgeport, CA		Sonora Junction, CA	
Elevation: 598.4 m	**Location:** 38.25°N, 119.22°W	**Elevation:** 639.7 m	**Location:** 38.4°N, 199.5°W
Date	**Precipitation (cm)**	**Date**	**Precipitation (cm)**
28 June 2011	0	28 June 2011	1.02
29 June 2011	0	29 June 2011	0
30 June 2011	0	30 June 2011	0
1 July 2011	trace	1 July 2011	trace
2 July 2011	0	2 July 2011	0
3 July 2011	0	3 July 2011	0
4 July 2011	0	4 July 2011	0
5 July 2011	0	5 July 2011	0
6 July 2011	0	6 July 2011	0
7 July 2011	0	7 July 2011	0
8 July 2011	0	8 July 2011	0
9 July 2011	0	9 July 2011	0
10 July 2011	0	10 July 2011	0
11 July 2011	0	11 July 2011	0
12 July 2011	0	12 July 2011	0
13 July 2011	0	13 July 2011	0

3.1. ASTER Data Processing

With the constraints mentioned, the ASTER diurnal pair dated from 10 July 2011 was used to create the ATI product for this study. The 10 July (day) image (Scene ID: AST_09T_00307102011185047) was collected at 18:50:47 GMT (11:50:47 local time) with a solar azimuth angle of 131.06° and a solar elevation angle of 68.11°. The 11 July (night) image (Scene ID: AST_09T_00307112011055433) was acquired at 05:54:33 GMT (22:54:33 local time on 10 July). Therefore, there was a 12:03:46 absolute time difference between the pair.

All data were obtained from the ASTER Level 2 (L2) on-demand processing pathway at the Land Processes Distributed Active Archive Center (LP DAAC) [71]. The ASTER L2 atmospherically-corrected TIR radiance data serve as the input product to derive the kinetic temperature images. An emissivity of 0.96 was used as a maximum assumed value in order to separate temperature and emissivity from the ASTER thermal infrared radiance images based upon previous spectral studies of glassy rhyolite [72,73]. The temperature difference product was created from these data (Figure 4). The standard L2 atmospherically corrected VNIR reflectance product was converted to albedo assuming no preferential directional scattering (generally valid on the rough and moderate albedo rhyolite surfaces) and calculated by averaging the three ASTER VNIR reflectance images. All VNIR data were down-sampled from 15 to 90 m/pixel to match the TIR resolution. The $(1 - a)$ product, where a is the albedo, was calculated and the image pair geographically aligned by rotating each to north and cropping the images to identical UTM coordinates. Precise pixel alignment was maintained throughout to ensure accurate comparison of the same pixel area. Once aligned and spatially matched, the temperature difference and complement of the albedo products were used to create the final ATI image using Equation (2) (Figure 5).

It should be noted that no SWIR data were used in the albedo calculation because of the failed system two years prior. The lack of SWIR for calculation of broadband albedo creates only minor errors for this analysis. The SWIR reflectance of glassy rhyolite lava and the rhyolitic mantling material are spectrally-similar across the SWIR wavelength region [74]. Therefore, no non-uniform spectral differences are expected between the lava and the mantling material with the lack of the SWIR data.

Including the SWIR (if it were available) would have therefore only slightly lowered the $(1 - a)$ term thus making the overall ATI calculation marginally lower throughout the image.

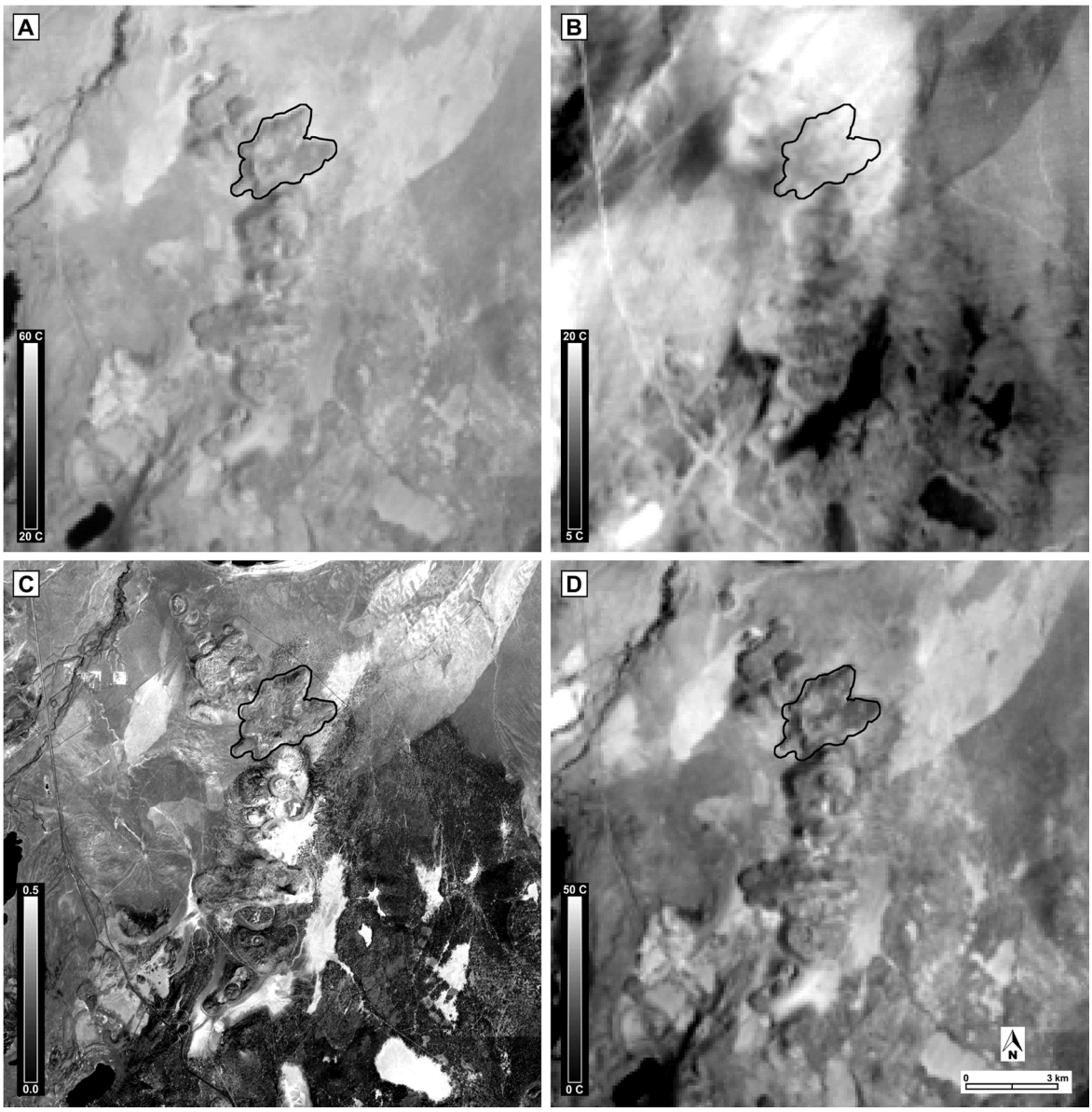

Figure 4. ASTER data products used to compile the apparent thermal inertia image. (**A**) Atmospherically-corrected, daytime surface kinetic temperature (ASTER level 2 AST_08 product) acquired on 10 July 2011 at 11:50:47 PDT; (**B**) Atmospherically-corrected nighttime surface kinetic temperature (ASTER level 2 AST_08 product) acquired on 10 July 2011 at 22:54:33 PDT; (**C**) Visible/Near Infrared surface albedo acquired at the same time as (**A**); (**D**) Temperature difference product (day − night).

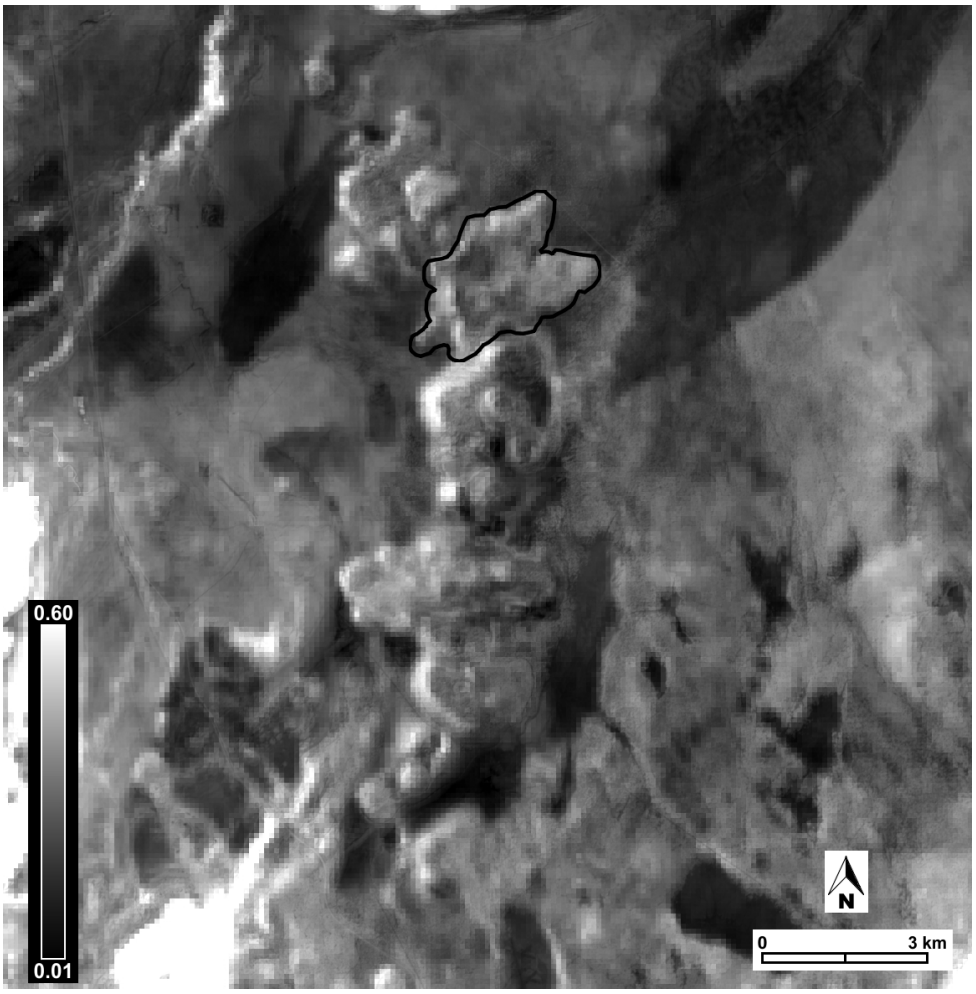

Figure 5. Apparent thermal inertia image derived for this study from the data shown in Figure 4. June Lake (**lower left**) and northwest-facing steep slopes have very high ATI values, whereas large, non-vegetated pumice deposits and old fire scars (**upper right**) (exposing the underlying pumice) have the lowest ATI values. Note that North Coulee has a range of ATI values 942 consistent with the preliminary work of Ramsey and Crown (2010) (see Figure 3).

3.2. Field Approach

The ATI image created for this study, as well as the product created by Ramsey and Crown (2010) [4] as a proof-of-concept, were both used to help identify potential field targets (Figure 3). It was considered important to select a variety of sites with a diverse range of ATI values in order to validate surface roughness, surface fragment size, surface temperature, mantling thickness, and collect samples. The ASTER TIR emissivity data were also used independently of the ATI to select areas of interest for field sampling. The day and night infrared emissivity data were compared with the ATI image to select areas with different micron-scale roughness [8] and identify any potential compositional variability. However, this comparison showed that the emissivity data were generally unable to resolve the differences identified by the ATI approach. A detailed description of the field work is given in Section 9, "Supplementary Information".

3.3. Laboratory Analyses

Because it was important to describe a variety of textures and particle sizes, a broad selection of samples from areas with various degrees of mantling were analyzed to validate the ATI results. High-resolution laboratory thermal emission spectra of all samples were acquired at the Image

Visualization and Infrared Spectroscopy (IVIS) facility at the University of Pittsburgh following the fieldwork. A petrographic study of the samples was also conducted. A detailed description of the laboratory analyses is given in Section 9, "Supplementary Materials".

4. Results

4.1. Image Results

Ramsey and Crown (2010) [4] hypothesized that ASTER-derived ATI values correlate with the presence of mantling and therefore perhaps variations in mantling thickness (Figure 3). Figure 5 shows the calibrated ATI results for this study. Our new analysis improved upon the earlier study by focusing on specific small-scale ATI targets, comparing results to the emissivity variation (both from ASTER and the laboratory), as well as tracking any changes in those values with time. For the date range described here, statistically significant differences in ATI were found. For example, initial comparison of lowest ATI regions with the high-resolution image data showed that these areas correlate precisely to heavily mantled surfaces on the dome (e.g., smooth morphology, lack of shadowing and the presence of sparse vegetation). In comparison, blocky surfaces had higher ATI values, topographic variability indicated by the presence of shadows and no vegetation. Furthermore, the ATI results indicate a similar correlation on the other domes and flows along the chain, although these were not visited during the field campaign.

4.2. Field Results

The calibrated ATI image was first used to identify the areas of interest for the field validation, with a wide variety of potential sites chosen that had different values of ATI, spanning the full range in ATI calculated. A subset of the selected field sites can be found in Figure 6 with data from all sites presented in Table 2. Comparison of high-resolution orbital images and the ATI image also helped to further constrain the choice of sites.

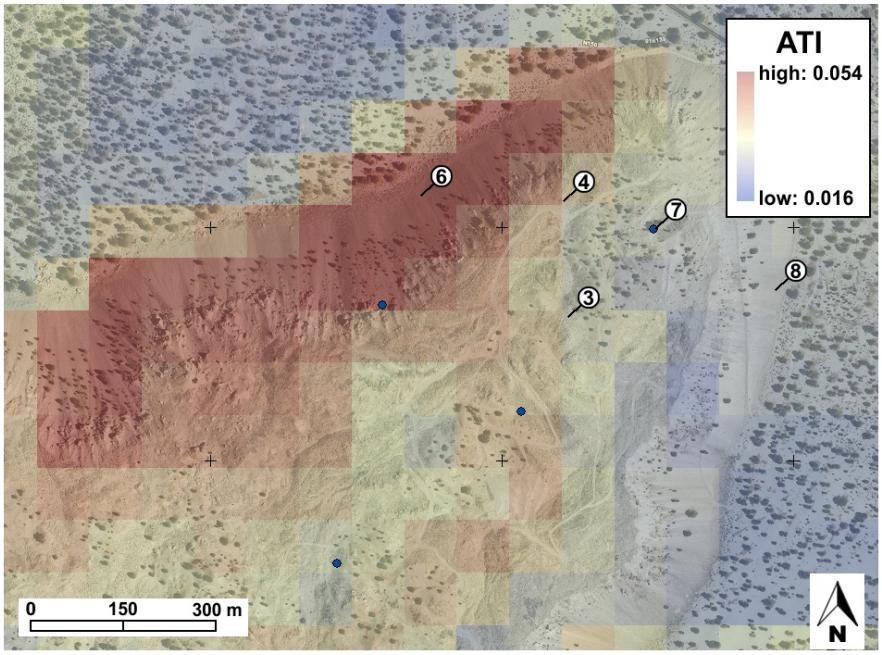

Figure 6. ATI draped over a high-resolution Digital Globe image (within Google Earth) of the northeast lobe of North Coulee. Blue dots indicate proposed field sites prior to the fieldwork being conducted. The numbered pins denote visited sites with associated field data. Note the very different ATI behavior on the northwest versus the southeast facing slopes. Figure created in ArcGIS 10 using Bing Maps layer.

Table 2. Characterization of the 13 targeted field sites in the study. Sorting and grain size determined after analysis using a petrographic microscope.

Site 1	
Average fragment size (cm):	0.5–1.0
Mantling depth (cm):	8.0–16.0
ATI value (×100):	**1.960**
General composition:	rhyolitic *(80% pumice/20% obsidian)*
Sorting degree:	well-sorted
Surface temperature (°C):	17.0
Local time:	10:15 a.m.
Field description:	*Course, angular grains, sand to gravel-sized. Well-sorted.*
Site 2	
Average fragment size (cm):	1.0–2.0
Mantling depth (cm):	<10
ATI value (×100):	**2.317**
General composition:	rhyolitic
Sorting degree:	moderately-sorted
Surface temperature (°C):	30.0
Local time:	15:00 p.m.
Field description:	*Well-sorted pyroclastic deposits. Course, angular, sand to gravel-sized grains. Predominantly pumice in composition.*
Site 3	
Average fragment size (cm):	bimodal *(0.03 and 0.50)*
Mantling depth (cm):	not measured *(inaccessible)*
ATI value (×100):	**2.576**
General composition:	rhyolitic
Sorting degree:	very poorly sorted
Surface temperature (°C):	not measured *(inaccessible)*
Local time:	n/a
Field description:	*Poorly-sorted mixture of pumice, obsidian, and other dome rocks. Large variation in size, from small sand-sized grains to 0.5m blocks.*
Site 4	
Average fragment size (cm):	40.0
Mantling depth (cm):	0.0
ATI value (×100):	**2.860**
General composition:	rhyolitic *(pumice and obsidian boulders)*
Sorting degree:	well-sorted
Surface temperature (°C):	not measured
Local time:	n/a
Field description:	*Well-sorted large volcanic debris consisting of pumice obsidian, and other dome rocks. Large, angular blocks ~1 m.*
Site 5	
Average fragment size (cm):	<0.5
Mantling depth (cm):	<30
ATI value (×100):	**2.645**
General composition:	rhyolitic
Sorting degree:	well-sorted
Surface temperature (°C):	46.2
Local time:	~2:00 p.m.
Field description:	*Well-sorted pumice dune consisting of fine sand. Wind-deposited. Surrounded by slopes of larger volcanic fragments.*

Table 2. *Cont.*

Site 6	
Average fragment size (cm):	3.0–6.0
Mantling depth (cm):	none
ATI value (×100):	**2.850**
General composition:	rhyoltic
Sorting degree:	poorly-sorted
Surface temperature (°C):	n/a
Local time:	n/a
Field description:	*Poorly-sorted weathered slope debris. Fragments range from smaller rocks a few cm in diameter to large meter-sized boulders. Minimal mantling.*
Site 7	
Average fragment size (cm):	1.0–3.0
Mantling depth (cm):	20.0
ATI value (×100):	**2.777**
General composition:	rhyolitic *(pumice and obsidian boulders)*
Sorting degree:	poorly-sorted
Surface temperature (°C):	not measured
Local time:	n/a
Field description:	*Poorly-sorted sand- and gravel-sized grains. About 30% is rhyolitic pumice boulders. Average boulder size ~0.3 m.*
Site 8	
Average fragment size (cm):	4.0
Mantling depth (cm):	none
ATI value (×100):	**2.461**
General composition:	rhyolitic
Sorting degree:	poorly-sorted
Surface temperature (°C):	n/a
Local time:	n/a
Field description:	*Poorly-sorted debris weathered off the east slope. 70% pumice 30% obsidian. Most fragments ~3–5 cm in size. Larger fragments ~15–20 cm.*
Site 9	
Average fragment size (cm):	1.0
Mantling depth (cm):	n/a
ATI value (×100):	**2.555**
General composition:	rhyolitic
Sorting degree:	well-sorted
Surface temperature (°C):	n/a
Local time:	n/a
Field description:	*Well-sorted wind-deposited pumice sediment. Some outcrops of larger volcanic debris.*
Site 10	
Average fragment size (cm):	<3
Mantling depth (cm):	None
ATI value (×100):	**2.731**
General composition:	rhyolitic *(pumice boulders)*
Sorting degree:	Intermediate
Surface temperature (°C):	22.5
Local time:	n/a
Field description:	*Slope with larger pumice fragments. Weathering of fragments varied. 80% pumice and 20% obsidian. Average grain size ~3 cm, varied.*

Table 2. *Cont.*

Site 11	
Average fragment size (cm):	0.5
Mantling depth (cm):	<30
ATI value (×100):	**3.340**
General composition:	rhyolitic *(90% pumice/10% obsidian)*
Sorting degree:	well-sorted
Surface temperature (°C):	55.7
Local time:	11:45 a.m.
Field description:	*Very well sorted rhyolitic grains. Some obsidian grains. High ATI value probably the result of sun angle/shadowing on western slopes.*
Site 12	
Average fragment size (cm):	40.0
Mantling depth (cm):	None
ATI value (×100):	**2.943**
General composition:	rhyolitic *(pumice and obsidian boulders)*
Sorting degree:	well-sorted
Surface temperature (°C):	not measured
Local time:	n/a
Field description:	*Well-sorted rhyolitic boulders with minimal mantling.*
Site 13	
Average fragment size (cm):	4.0–6.0
Mantling depth (cm):	n/a
ATI value (×100):	**2.697**
General composition:	rhyolitic *(70% pumice/30% obsidian)*
Sorting degree:	poorly-sorted
Surface temperature (°C):	22.5
Local time:	9:00 a.m.
Field description:	*Poorly sorted slope debris. All grains and blocks very angular. Debris ranges from fine sand to >0.3 m fragments.*

Field data were acquired at a total of 13 sites both on the dome surface as well as around the perimeter. The results are described in detail for four of these sites to give a representative description of the variability encountered as well as the measurement approach employed. In general, the results (Table 2, above) from the field validation at North Coulee correlate very well with the image results (Figures 7 and 8). Areas of low ATI (Figure 7, Site 1) predominantly consisted of tephra deposits; whereas areas of higher ATI were comprised exclusively of non-mantled larger (>10 cm) rhyolite pumice and obsidian blocks (Figure 8, Site 4). Zones with intermediate ATI commonly consisted of either homogenous intermediate-sized particles (1–4 cm) (e.g., Figure 7, Site 2) or a bimodal distribution of block sizes from fine to coarse (e.g., Figure 8, Site 3). A detailed explanation of the field sites is given in Section 9, "Supplementary Materials".

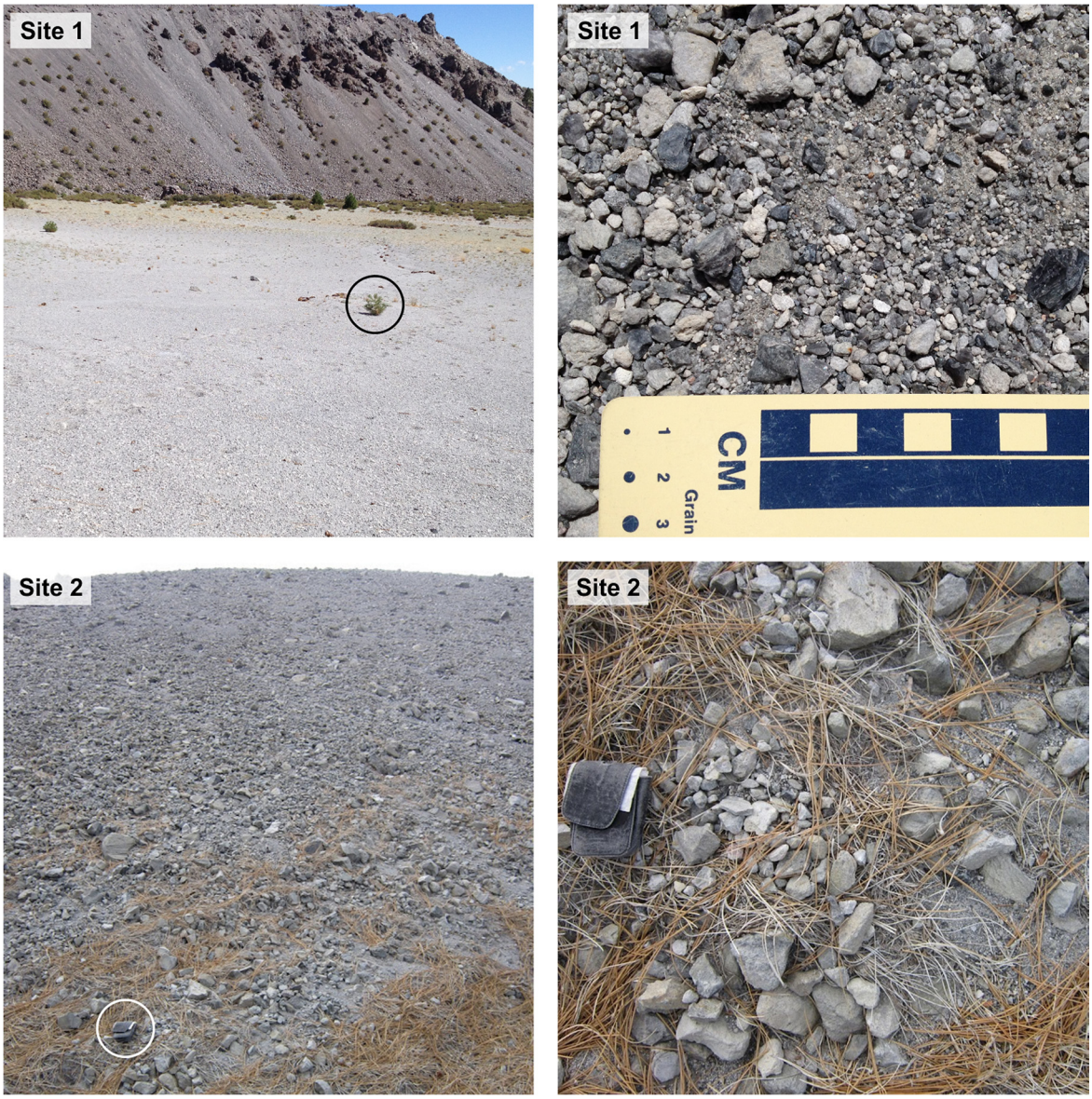

Figure 7. Field photographs of Site 1 (**upper row**) and Site 2 (**lower row**) with context images shown in the left hand column and close-up images in the right hand column. Site 1 is a large pumice plain at the base of the coulee (black circle shows an approximate 30 cm high pine tree sapling for scale). The particle size for this site is 1 cm or less. Site 2 is a mantled location on the coulee (white circle shows an approximate 12 cm camera case for scale). Note the bimodal distribution of particle sizes at this site with the largest particles exceeding 12 cm.

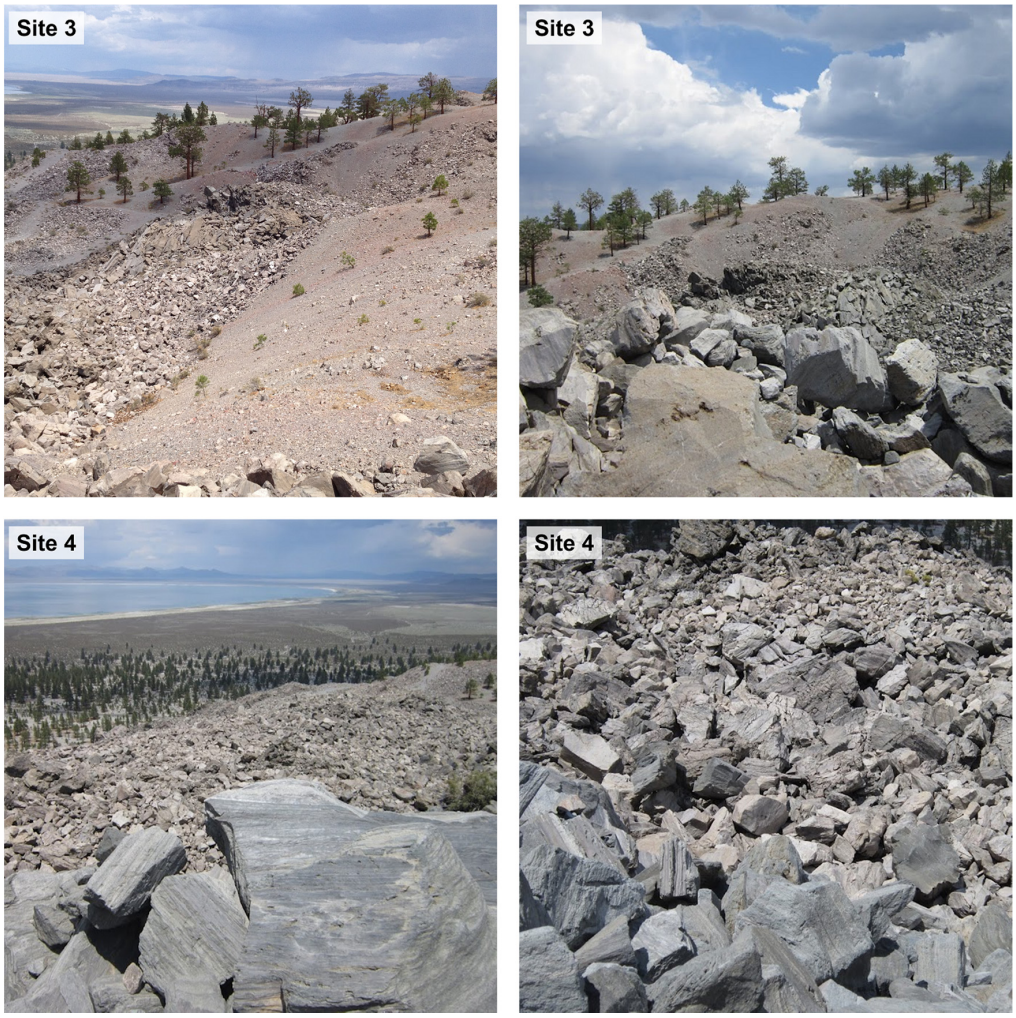

Figure 8. Field photographs of Site 3 (**upper row**) and Site 4 (**lower row**) with context images shown in the left hand column and close-up images in the right hand column. Site 3 has a strongly bimodal particle size consisting of mantling similar to Site 2 as well as a non-mantled primary lava flow surface (blocks). Site 4 is a completely non-mantled location on the coulee. The block size distribution measured along a transect for this site is shown in Figure 9.

4.3. Laboratory Results

Laboratory thermal infrared emissivity spectra were acquired of the field samples. Nearly all had identical spectral morphology with a prominent absorption feature at 9.1 microns (ASTER TIR band 12) indicative of high-silica glass [75]. However, one sample spectrum had a much deeper feature; likely caused either by fewer highly-vesicular fragments and/or the larger particle size of the sample (~3–5 cm), each of which would minimize photon scattering and produce deeper spectral features [73]. The 9.1 micron emissivity values for each sample were plotted against the corresponding ATI value extracted for the same pixel, with no correlation found (Figure 10). This result is not surprising for a surface consisting of approximately the same composition (rhyolite) and widely varying particle size (mm-scale fragments to m-scale blocks), varying textures (*i.e.*, glassy obsidian and highly vesicular pumice), and/or micron scale roughness values [73]. This homogeneity in the composition and heterogeneity in the textures and particle sizes limits the use of emissivity alone to determine details of the surface properties and highlights the importance of ATI for mantled surfaces such as these.

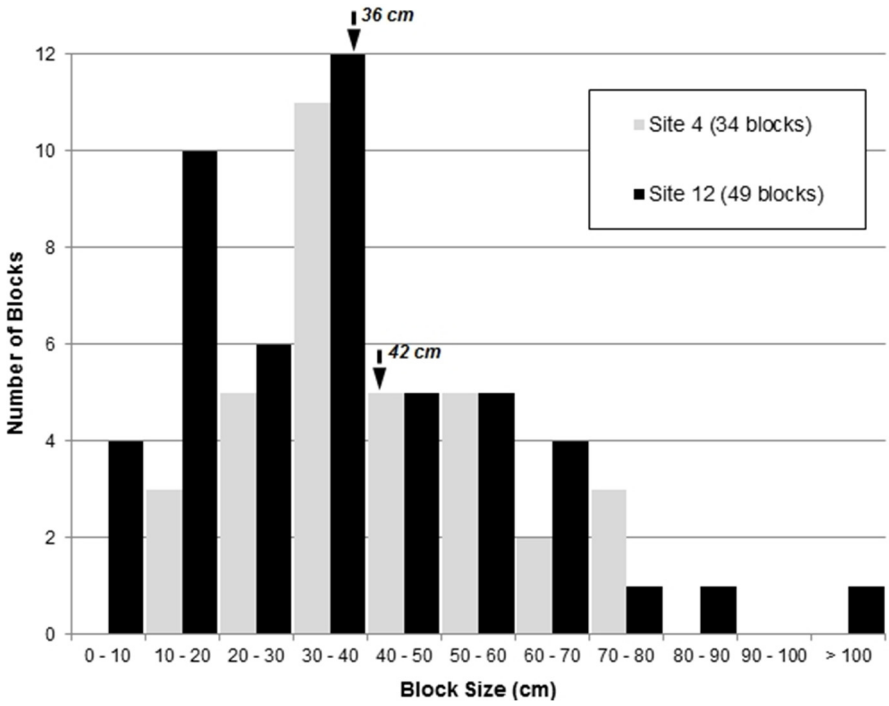

Figure 9. Block size distributions for the non-mantled Site 4 and Site 12. The average block size for each is denoted with the arrows.

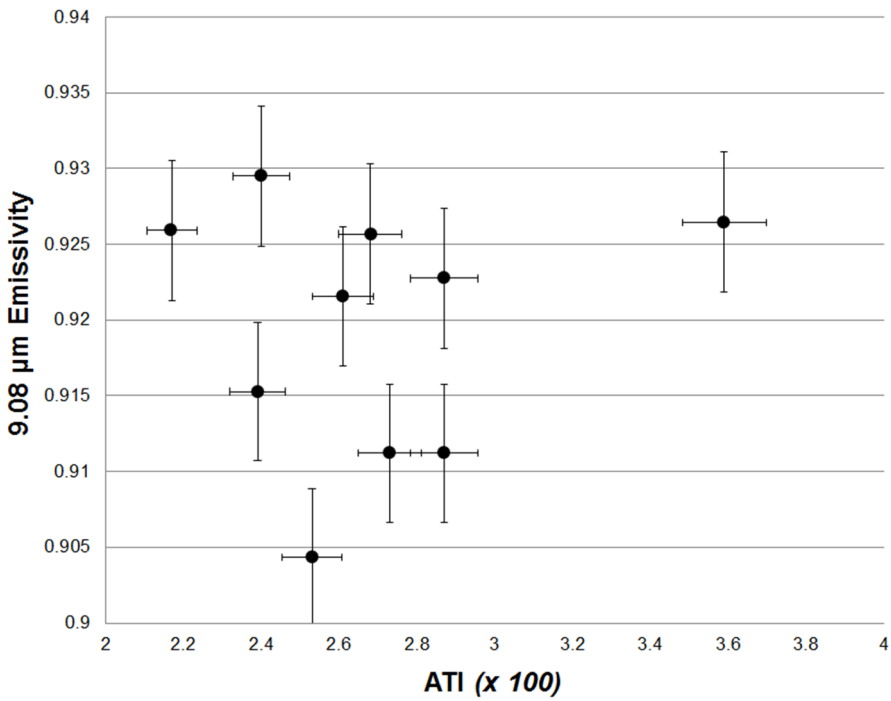

Figure 10. ASTER TIR band 12 (9.1 micrometers) surface emissivity (Level 2, AST_05) versus ATI for various the field sites. The lack of correlation is a direct result of very similar composition (pumiceous rhyolite lava and air fall pumice) reflected in the emissivity with very different particle sizes (pyroclastic air fall to blocks) reflected in the ATI. Error bars denote the standard error associated with the AST_05 product and the composite error in the derived ATI.

The petrographic analysis of the same samples confirmed the findings from the satellite and field analyses. Particulate samples were prepared on a slide and point counts conducted on a 5 by 5 cm grid using a petrographic microscope [49,50]. The composition was found to be very similar for most samples with ratios of ~3:1 rhyolitic pumice tephra to obsidian glass fragments with visible vesicles seen in two-thirds of the samples. The majority of the samples from the low ATI sites contained well-sorted particles with an average grain size of ~25 mm. Several samples contained larger (~150 mm) well-sorted grains, but these are less common. Four samples are considered poorly sorted, with grain sizes ranging from 6 mm to as large as 30 cm.

4.4. Data Integration

To further explore the variations observed in the thermophysical properties, the ATI data were compared to field and laboratory determined composition and particle size by creating a dome-wide particle size map (Figure 11). This is the first terrestrial application to confirm the relationship between ATI and particle size in volcanic environments. ATI values less than 2.3×10^{-2} at North Coulee were confirmed to be associated with the pyroclastic tephra deposits. For example, Site 1 had an ATI value of 1.9×10^{-2} ATI with an average measured grain size between 5–10 mm, and a mantling thickness of ~16 cm. Ground validation also confirmed sites with ATI values greater than 2.3×10^{-2} are not entirely mantled (e.g., Site 4). These are either associated with homogeneous smaller block size surfaces or are an aerial mixture of mantled surfaces and larger boulders (e.g., Site 3). However, the average particle size increases and correlates well with ATI values above 2.8×10^{-2}. Pixels with values greater than this threshold are entirely associated with mantle-free flow surfaces consisting of larger lava blocks. Surfaces with average block sizes >~20 cm all result in very similar ATI, which indicates this block size is near the upper limit of the ATI sensitivity.

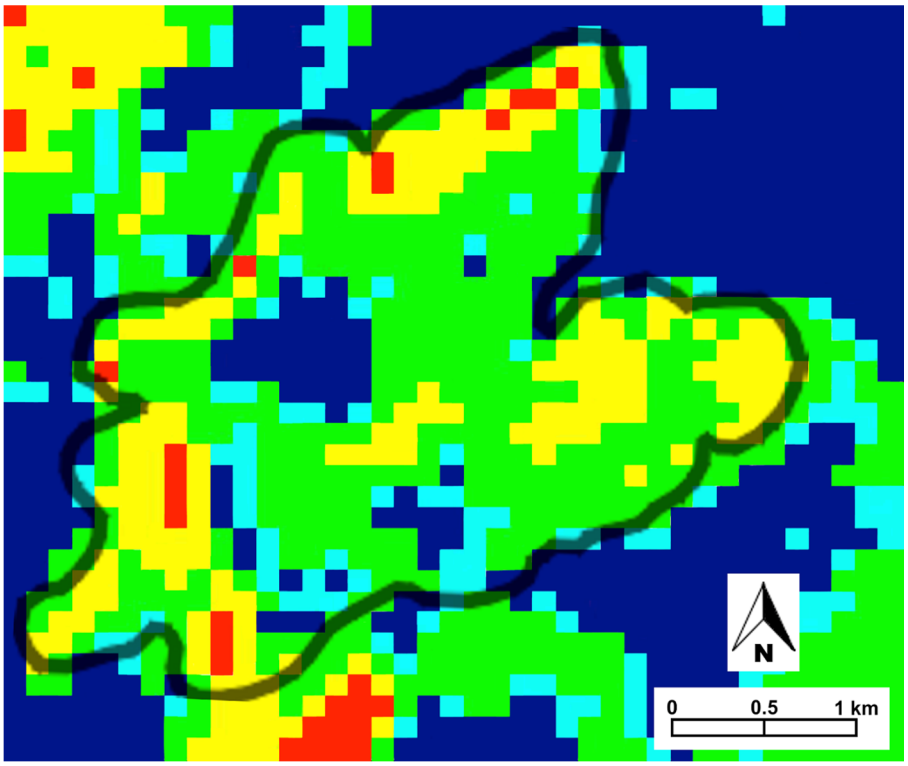

Figure 11. Average pixel-integrated particle size map of the North Coulee 972 flow derived from extensive field measurements and related back to the calculated ATI, with blue (<1 cm), cyan (1 cm–3 cm); green (3 cm–500 cm); yellow (500 cm–1.0 m); and red (>1 m). The approximate flow boundary is shown by the black outline. Map created from ATI image.

As noted previously, this ATI approach results in inaccurate values for pixels containing steep topography and hence, shadowing. Large-scale (greater than the pixel-scale) shadowing is found primarily on the north and northwestern flow fronts. These shadows lower the amount of VNIR reflectance and daytime temperature of the surface thereby producing much higher ATI values. Because the main focus of this study was the mantled flow surfaces themselves and not the flow fronts, we did not correct for this shadowing. Work by Simurda and Ramsey (2014) [76] is addressing these shadowing errors using image and ground based digital elevation models (DEMs) to calculate and remove the effects of both large-scale and sub-pixel roughness elements.

5. Discussion

5.1. Terrestrial Applications

The distribution of grain and block sizes on the surface of North Coulee is related to both the emplacement of the high-silica rhyolite flow itself as well as subsequent volcanic activity in the region. Post-emplacement mechanical weathering would have had little effect on the block size distribution due to the young age of these flows. However, emplacement of the high-viscosity lavas and stress conditions during flow have been shown to break larger blocks into smaller, sub-meter fragments with distance from the vent [77]. Vent regions generally contain the largest average block size, whereas ridged zones further from the vent will have the smallest average block size due to compressional stresses. The non-mantled surfaces of North Coulee follow a similar pattern in the ATI result. Sites 1 and 2 (lower ATI) are situated near southern ridges, and contain homogenous, smaller block sizes. Whereas sites 3 and 4 (higher ATI) are further north on the dome and closer to the vent region [54].

During dome emplacement the higher temperature lava below the surface inhibits fracturing and also promotes the formation of distinct flow stratigraphy and volcanic breccia through annealing [78]. The process of breccia formation and flow stratigraphy formation are both evident at various locations around North Coulee where large breccia blocks and obsidian outcrops are visible. Areas where these outcrops occur in non-shadowed regions produced some of the highest measured ATI values. Weathering and gravitational collapse of these blocks has produced fragmental material that also has a higher ATI than the detrital material.

Complicating the direct relationship between ATI, particle size, and dome emplacement processes at North Coulee is the presence of the overlying mantling deposits, which was the focus of this study. Emplaced during eruptions of younger domes, these deposits mask the flow surface in many areas but also create an ideal test location for the Mars flows. High ATI values ($>3.0 \times 10^{-2}$) are generally found in areas dominated by large obsidian and rhyolite boulders. Conversely, lower ATI values ($<2.3 \times 10^{-2}$) are indicative of extensive finer-grained pyroclastic mantling. Pixels with ATI values intermediate to this range generally can be divided into two categories: homogenous, moderately-sized particles (Figure 2, Site 2) or heterogeneous mixing of fine-grained mantling deposits with unmantled larger blocks (Figure 2, Site 3). Within this first group, ATI values between 2.3×10^{-2} and 2.5×10^{-2} generally corresponded to surfaces with particles ranging from 1 to 4 cm, whereas larger ATI values corresponded to blocks greater than 5 cm.

However, the correlation between ATI and emissivity is poor; a result similar to the studies of mantled flows on Mars [4,17,62]. This lack of correlation can be explained by the composition and texture of the surface materials. The domes and mantling deposits at North Coulee all consist of high silica rhyolite of various block and particle sizes and surface textures. Therefore, emissivity is not a reliable indicator to distinguish mantled from non-mantled surfaces, nor extract the fragment size or vesicular texture because of similar composition and vesicular state [73].

Distinguishing non-mantled lava flows from flows that contain some level of volcanic and/or eolian mantling on Earth is possible with the appropriate caution and validation using this approach. ATI relies on diurnal temperature measurements, which are affected by atmospheric conditions such as changes in humidity, precipitation, surface cooling by winds, as well as degassing and heat loss on

active flows and domes. Accurate atmospheric correction is important and considered to be relatively well understood for terrestrial TIR corrections. However, active domes on Earth will produce gases that are not commonly corrected in standard atmospheric models such as MODTRAN and have temperatures well above the average background. This internal heat would complicate the normal diurnal heating and cooling process, thereby making ATI more complex to interpret. Finally, the presence of vegetation on older domes (if extensive) could lead to erroneous results. Future work using this approach in terrestrial applications should therefore be focused mainly on younger flows that have cooled and have sparse vegetation cover. In addition, an accurate knowledge of the recent precipitation and climate conditions prior to the data collection is important.

It should be noted that more robust ATI calculations can be implemented using various additions to the basic ATI equation. For example, the inclusion of simple scaling factors [9] through a much more rigorous implementation to convert ATI to approximated actual thermal inertia [41]. Scheidt *et al.* (2010) [9] includes two variables (n and c) in the calculation of ATI using: $ATI = nc\ (1 - a)/\Delta T$, where n and c are correction factors to account for variations in solar flux with latitude and solar declination [79]. The effects of these scaling factors at this latitude and time of year are generally quite small and would have no effect on reducing the larger scale shadowing errors. Therefore, their addition is not deemed critical to this study, but may be important for applications at other locations.

5.2. Applications to Mars

The application of this type of approach for mantled lava flows on the SW apron of Arsia Mons and within the plains of Daedalia Planum in the southern part of the Tharsis region of Mars was initially explored by Ramsey and Crown (2010) [4] and Crown *et al.* (2012) [16]. Finding an approach to accurately discriminate regions of mantling on volcanic surfaces from the underlying lava flows using a thermophysical methodology has the potential to greatly improve the understanding of the compositional and volcanic history of these regions. However, the ATI approach should also be compared to model-based theoretical thermal inertia results in order to determine its applicability for Mars. For example, ATI derived from THEMIS could be used as simpler alternative to model-derived thermal inertia with the results being used to quickly determine inter-pixel mixing and homogeneous cover of coarser grained particles [34]. The success of using ATI to determine grain and block size of the North Coulee flow indicate that an ATI analysis of the flow fields of Arsia Mons and surrounding regions could be useful. The similarity between the two regions and the success of ATI analysis on Earth warrant an analogous study on Mars.

6. Conclusions

Initial applications were successful in utilizing apparent thermal inertia to distinguish mantled from non-mantled terrestrial volcanic surfaces and directly link ATI to particle size for the Mono Craters and Domes. For this study, mantled regions had a calculated ATI of $<2.3 \times 10^{-2}$, whereas blocky non-mantled deposits had an ATI value above 3.0×10^{-2}. ATI findings were able to distinguish the average grain size of these mantling deposits adding further fidelity to the study. A mantled pixel with a very low (1.6×10^{-2}) value correlated with an average grain size of ~0.5 cm in the field, whereas another mantled pixel with an ATI value of 2.3×10^{-2} had an average grain size of 1–2 cm. The sensitivity of this ATI approach is obvious and therefore valuable for mapping flows on Earth that are partially-mantled or that contain a wide range of particle/block sizes due to flow emplacement conditions. The use of ATI is also an asset in hazardous or inaccessible terrain where ground validation becomes impossible or dangerous. However, pixel mixing and larger-scale shadowing can hinder accurate interpretation of ATI results depending on image resolution and caution should be taken where interpreting these results without direct field observations or validation using other high-resolution images. For example, moderate ATI values at the MCD indicate either heterogeneous (mixed) particle sizes or a homogenous pixel of an intermediate particle size. These

cannot be uniquely separated with the ATI data alone. In these cases, ground validation (either on-site or from higher-resolution aerial or satellite images) is required until the development of a more nuanced ATI model. Finally, very high ATI values in steep topography (particularly on slopes opposite the solar azimuth angle) are likely the result in a large amount of pixel-integrated shadowing. These are typically easy to identify and ongoing work is addressing these errors through incorporation of a DEM into the ATI calculation. Future work using ATI should also address mantling thickness using a layered model to estimate thicknesses and attempt to decouple the effects of layering and or accurately identify areas of the lava that protrude through the mantling deposit.

The success of this terrestrial ATI study bodes well for its inclusion in research identifying mantled surfaces in volcanic regions on Mars. Using ATI in addition to modeled thermal inertia allows areas of mantling on Mars to be properly classified, mantling thickness to be constrained, and the percentage of checkerboard mixing between mantled deposits and the underlying lava to be determined. This will then allow spectral analysis to be concentrated on just those regions of exposed lava with minimal to no mantling, which enables textural and compositional analysis both down flow from the vent as well as across different flow units comprising the larger flow field. Where combined with geologic mapping and relative age dating, this integrated analysis becomes an important tool for interpreting the larger volcanic history of the flow field under study (as opposed to the eolian history of the mantling). Ideal study sites include the lava flow fields of southern Arsia, which display a wide range of thermophysical behavior with some flows exhibiting a thermophysical response consistent with a complete dust cover and others appearing to be dust-free. Even more confounding are flows that do not show any consistent thermophysical behavior throughout the day by staying consistently cool or warm [4]. Therefore, identifying these mantling deposits, their thickness, their separation from the underlying rocks, and the eventual mapping of the underlying lava composition should provide a much greater insight into this relatively young volcanic field on Mars and the subsequent eolian modification of these regions.

Supplementary Materials:

Details of Field Approach

Fieldwork was conducted on the North Coulee flow from 13–17 July 2012, and included detailed measurements at 13 sample sites across the dome surface and around the perimeter (Table 2, above). Sites were selected on the North Coulee flow with high values of ATI as well as at numerous low ATI targets assumed to be mantled (Figure 6). Data collection included photographs, GPS location, surface roughness measurements, sediment descriptions, direct contact temperature measurements using a thermocouple at the surface and three depths where possible (1 cm, 15 cm, and 25 cm), measurement of the large block sizes, as well as sample collection for later TIR laboratory spectral analysis. Samples and locations were selected specifically to be representative of the deposits within the 90-meter ASTER TIR pixel and the dome as a whole. If a layer of mantling material covered a site, samples of the mantling deposit and underlying material (buried mantled deposits or dome rock) were obtained. The depth of the mantling layer was also measured (where possible). If a site had no mantling deposits, the block sizes were measured along transect lines and a representative sample was collected for later laboratory analysis. Contiguous rock-mantle contacts at the surface were mapped by walking the contact using a Trimble XRS real-time differential Global Position System (GPS) unit with an accuracy of ~30 cm in order to later calculate the areal proportion of mantling within a given pixel. In addition, a complete and detailed survey of an ASTER TIR pixel (90 m^2) was conducted at one site to assess the degree of surface variability and improve the confidence in the sampling strategy at the other sites. This pixel calibration survey consisted of visual observations taken at one meter intervals in a crosswise transect from one corner to the opposite corner. Surface components (e.g., percent vegetation, vegetation type, vegetation height, mantling percentage, average particle size of the mantling material, composition, *etc.*) were all logged and later averaged over the entire pixel to gain a thorough understanding of the sub-pixel diversity.

Details of Laboratory Analyses

The Nicolet Nexus 670 spectrometer used in laboratory analyses has a 2 wavenumber spectral resolution between 2000 and 400 wavenumber (~5–25 μm). A thorough account of the measurement approach and data calibration processing can be found in Ruff *et al.* (1997) [80]. Several grams of particulate sample were placed in 2.5 cm diameter cups and heated to 80 °C in a temperature-controlled oven for a 24-h period. Each sample was then placed on a controlled heating stage within a CO_2 and H_2O purged glovebox. The spectral spot size of approximately 2 cm assured a well-represented spectrum of each mixed sample. Each analysis took ~5 min resulting in a spectrum with a signal to noise of ~800. The spectra were also compared to the corresponding

five-point TIR emissivity spectra obtained from the ASTER emissivity of the pixel that contained that sample. Both sets of spectra (laboratory and ASTER) were deconvolved using the approach of Ramsey and Christensen (1998) [7] with obsidian and blackbody end-members to determine surface vesicularity [7,73]. In addition to the spectral analysis, all samples were viewed under a petrographic microscope and point counts made on a five by five centimeter grid to constrain both texture and grain size.

Detailed Results of Field Sites

Site 1 is located at the base of the flow front on the southeastern side of North Coulee (see Figure 3 for location, Figure 7 for ground images). A 90 m-pixel survey was conducted at this site to validate the ATI results, which had the lowest ATI in the MCD scene (1.6×10^{-2}). Considering this location had an ATI value less than the maximum (ATI = 2.3×10^{-2}) for a mantled surface on the dome, it was assumed that this pixel contained a very fine-grained deposit with a thick mantling depth. This was verified by the pixel survey, with the site having an approximate mantling depth of 16 cm and an average grain size of 0.5 to 1.0 cm with grains as small as 13 mm. Field investigation found Site 1 to be relatively homogenous in composition and particle size across the surveyed region, with no large blocks, vegetation or slopes. It was therefore considered the ideal calibration pixel for the later analyses of other sites.

The location of Site 2 (Figure 7) is on the eastern section of a large pumice deposit on the western slope of North Coulee. The ATI of 2.3×10^{-2} is considered to be at the upper end of the range of a well-mantled surface. Ground analysis here revealed the average grain size to be larger (1–2 cm) than Site 1, with grains as small as ~2 mm. This site also is fairly homogenous, but closer to large boulder piles and with no measureable vegetation.

Site 3 (Figure 8) is located on the northeastern lobe of North Coulee and is an example of bimodal particle-size areal mixing that resulted in a pixel of moderate ATI (2.6×10^{-2}). Within this pixel area, large (~0.5 m) blocks dominated one half, whereas finer-grained pyroclastic material covered the remainder. Several moderately high pine trees (~10 m) and small shrubs were found growing in the fine-grained material. However, this vegetation comprised no more than 2%–3% of the total area and therefore did not affect the ATI result in a measurable way. The average grain size was not measured here due to rough terrain but was observed to fall between the size of the blocks (~0.15 m) and pyroclastic particles (1–4 cm).

Site 4 (Figure 8) is also located on the northeastern lobe of North Coulee, about 100 m north of Site 3 near the edge of the northern flow front. This region had one of the higher calculated ATI values (2.9×10^{-2}) of all surfaces on North Coulee. The blocks in this area are larger than previous sites. Each block was measured along a 50 m transect and resulted in an average size of 40 cm, with the largest measuring 720 cm and the smallest being 170 cm (see Figure 9 for block size measurements).

Other sites included an outlying dome on the southwest edge of the coulee with a large pumice deposit (Figure 3, Site 10) and a high ATI value, as well as plains of fine-grained pumice deposited near the western edge of North Coulee (Figure 3, Site 9). The large pumice deposit was examined specifically because the higher ATI should be indicative of larger blocks or well-cemented deposits, counterintuitive to what was presumed to be at this site. The deposit was found to be comprised of loosely-consolidated, coarse-grained pyroclastic granules (~1–5 cm) deposited on a steep slope. Because of the position of this deposit on the western side of the dome (and the fact that other western and northern slopes have higher ATI), the elevated ATI was presumed to be caused mainly by shadowing produced from the slope face. Site 9 was located on a region of the dome with the most pervasive mantling. It contained very well-sorted, finer-grained, wind-deposited pumice with outcrops of larger volcanic debris protruding through. The larger outcrops were ~10% of the pixel area and raised the ATI result into the intermediate range (2.6×10^{-3}). Locations such as these were seen as the most similar Mars analog found on the North Coulee flow.

Acknowledgments: Funding for this research was made possible through the NASA Planetary Geology and Geophysics (PGG) Program (grant NNX11AP17G). The quality and clarity of this manuscript were greatly improved by reviews from Gaetana Ganci, Gabor Kereszturi and David Pieri. The authors would also like to thank Anna Downey (PGG Undergraduate Research Program student) for her assistance during the fieldwork and research preparation.

Author Contributions: Michael Ramsey and David Crown conceived and designed the experiments. Mark Price performed the experiments. Mark Price and Michael Ramsey analyzed the data. Michael Ramsey contributed materials and laboratory equipment. Mark Price wrote the paper.

Conflicts of Interest: The authors declare no conflict of interest.

References and Notes

1. Malin, M.C.; Edgett, K.S. Mars Global Surveyor Mars Orbiter Camera: Interplanetary cruise through primary mission. *J. Geophys. Res.* **2001**, *106*, 23429–23570. [CrossRef]
2. Christensen, P.R.; Bandfield, J.L.; Hamilton, V.E.; Ruff, S.W.; Kieffer, H.H.; Titus, T.N.; Malin, M.C.; Morris, R.V.; Lane, D.M.; Clark, R.N.; *et al.* Mars Global Surveyor Thermal Emission Spectrometer experiment: Investigation description and surface science results. *J. Geophys. Res.* **2001**, *106*, 23823–23871. [CrossRef]

3. Bandfield, J.L.; Hamilton, V.E.; Christensen, P.R.; McSween, H.Y. Identification of quartzofeldspathic materials on Mars. *J. Geophys. Res.* **2004**, *109*. [CrossRef]
4. Ramsey, M.S.; Crown, D.A. Thermophysical and spectral variability of Arsia Mons lava flows. In Proceedings of the 41st Lunar and Planetary Science Conference, The Woodlands, TX, USA, 1–5 March 2010.
5. Hunt, G.R.; Vincent, R.K. The Behavior of Spectral Features in the Infrared Emission from Particulate Surfaces of Various Grain Sizes. *J. Geophys. Res.* **1968**, *73*, 6039–6046. [CrossRef]
6. Mustard, J.F.; Hays, J.E. Effects of hyperfine particles on reflectance spectra from 0.3 to 25 µm. *Icarus* **1997**, *125*, 145–163. [CrossRef]
7. Ramsey, M.S.; Christensen, P.R. Mineral abundance determination: Quantitative deconvolution of thermal emission spectra. *J. Geophys. Res.* **1998**, *103*, 577–596. [CrossRef]
8. Ramsey, M.S.; Fink, J. Estimating silicic lava vesicularity with thermal remote sensing: A new technique for volcanic mapping and monitoring. *Bull. Volcanol.* **1999**, *61*, 32–39. [CrossRef]
9. Scheidt, S.; Ramsey, M.; Lancaste, N. Determining soil moisture and sediment availability at White Sands Dune Field, New Mexico, from apparent thermal inertia data. *J. Geophys. Res.* **2010**, *115*. [CrossRef]
10. Scheidt, S.; Lancaster, N.; Ramsey, M. Eolian dynamics and sediment mixing in the Gran Desierto, Mexico, determined from thermal infrared spectroscopy and remote-sensing data. *Geol. Soc. Am. Bull.* **2011**, *123*, 1628–1644. [CrossRef]
11. Edgett, K.S.; Lancaster, N. Volcaniclastic aeolian dunes: Terrestrial examples and application to Martian sands. *J. Arid Environ.* **1993**, *25*, 271–297. [CrossRef]
12. Fenton, L.K.; Bandfield, J.L. Aeolian processes in Proctor Crater on Mars: Sedimentary history as analyzed from multiple data sets. *J. Geophys. Res.* **2003**, *108*. [CrossRef]
13. Johnson, J.R.; Christensen, P.R.; Lucey, P.G. Dust coatings on basaltic rocks and implications for thermal infrared spectroscopy of Mars. *J. Geophys. Res.* **2002**, *107*. [CrossRef]
14. Ruff, S.W.; Christensen, P.R. Bright and dark regions on Mars: Particle size and mineralogical characteristics based on thermal emission spectrometer data. *J. Geophys. Res.* **2002**, *107*. [CrossRef]
15. Bandfield, J.L. Effects of surface roughness and graybody emissivity on martian thermal infrared spectra. *Icarus* **2009**, *202*, 414–428. [CrossRef]
16. Crown, D.A.; Ramsey, M.S.; Berman, D.C. Morphologic and chronologic studies of lava flow fields in the southern Tharsis region of Mars. In Proceedings of the 43rd Lunar and Planetary Science Conference, The Woodlands, TX, USA, 19–23 March 2012.
17. Ramsey, M.S.; Crown, D.A.; Price, M.A. Decoupling lava flow composition and emplacement processes from eolian mantling deposits using thermal infrared data. In Proceedings of the 43rd Lunar and Planetary Science Conference, The Woodlands, TX, USA, 19–23 March 2012.
18. Price, M.A.; Ramsey, M.S.; Crown, D.A. Thermophysical characteristics of mantled terrestrial volcanic surfaces: Infrared analogs to the Arsia Mons flows. In Proceedings of the 44th Lunar and Planetary Science Conference, The Woodlands, TX, USA, 18–22 March 2013.
19. Crown, D.A.; Ramsey, M.S. Morphologic and thermophysical characteristics of lava flows southwest of Arsia Mons, Mars. *J. Volc. Geotherm. Res.* **2016**. under review.
20. Hardgrove, C.; Moersch, J.; Whisner, S. Thermal imaging of alluvial fans: A new technique for remote classification of sedimentary features. *Earth Planet. Sci. Lett.* **2009**, *285*, 124–130. [CrossRef]
21. Greeley, R. The Snake River Plain, Idaho: Representative of a new category of volcanism. *J. Geophys. Res.* **1982**, *87*, 2705–2712. [CrossRef]
22. Plescia, J.B. Morphometric properties of martian volcanoes. *J. Geophys. Res.* **2004**, *109*. [CrossRef]
23. Lang, N.P.; Tornabene, L.L.; McSween, H.Y., Jr.; Christensen, P.R. Tharsis-sourced relatively dust-free lavas and their possible relationship to Martian meteorites. *J. Volcanol. Geotherm. Res.* **2009**, *185*, 103–115. [CrossRef]
24. Terra | The EOS Flagship. Available online: terra.nasa.gov (accessed on 7 October 2015).
25. Yamaguchi, Y.; Kahle, A.; Tsu, H.; Kawakami, T.; Pniel, M. Overview of Advanced Spaceborne Thermal Emission and Reflectance Radiometer (ASTER). *IEEE Trans. Geosci. Remote Sens.* **1998**, *36*, 1062–1071. [CrossRef]
26. Edgett, K.S.; Malin, M.C. Martian sedimentary rock stratigraphy: Outcrops and interbedded craters of northwest Sinus Meridiani and southwest Arabia Terra. *Geophys. Res. Lett.* **2002**, *29*. [CrossRef]

27. Bandfield, J.L.; Feldman, W.C. Martian high latitude permafrost depth and surface cover thermal inertia distributions. *J. Geophys. Res.* **2008**, *113*. [CrossRef]
28. Price, J.C. Thermal inertia mapping: A new view of the earth. *J. Geophys. Res.* **1977**, *82*, 2582–2590. [CrossRef]
29. Palluconi, F.D.; Kieffer, H.H. Thermal inertia mapping of Mars from 60 S to 60 N. *Icarus* **1981**, *45*, 415–426. [CrossRef]
30. Jakosky, B.M.; Mellon, M.T.; Kieffer, H.H.; Christensen, P.R.; Varnes, E.S.; Lee, S.W. The thermal inertia of Mars from the Mars global surveyor thermal emission spectrometer. *J. Geophys. Res.* **2000**, *105*, 9643–9652. [CrossRef]
31. Fergason, R.L.; Christensen, P.R.; Kieffer, H.H. High-resolution thermal inertia derived from the Thermal Emission Imaging System (THEMIS): Thermal model and applications. *J. Geophys. Res.* **2006**, *111*. [CrossRef]
32. Kieffer, H.H.; Martin, T.Z.; Peterfreund, A.R.; Jakosky, B.M.; Miner, E.D.; Palluconi, F.D. Thermal and albedo mapping of Mars during the Viking primary mission. *J. Geophys. Res.* **1977**, *82*, 4249–4291. [CrossRef]
33. Edgett, K.S.; Christensen, P.R. The particle size of Martian aeolian dunes. *J. Geophys. Res.* **1991**, *96*, 22765–22776. [CrossRef]
34. Christensen, P.R. Martian dust mantling and surface composition: Interpretation of thermophysical properties. *J. Geophys. Res.* **1982**, *87*, 9985–9998. [CrossRef]
35. Fink, J.H.; Manley, C.R. Origin of pumiceous and glassy textures in rhyolite flows and domes. In *The Emplacement of Silicic Domes and Lava Flows*; Fink, J.H., Ed.; Geological Society of America Special Paper; Geological Society of America: Boulder, CO, USA, 1987; Volume 212, pp. 77–88.
36. Putzig, N.E.; Mellon, M.T.; Kretke, K.A.; Arvidson, R.E. Global thermal inertia and surface properties of Mars from the MGS mapping mission. *Icarus* **2005**, *173*, 325–341. [CrossRef]
37. Rogers, A.D.; Christensen, P.R.; Bandfield, J.L. Compositional heterogeneity of the ancient Martian crust: Analysis of Ares Vallis bedrock with THEMIS and TES data. *J. Geophys. Res.* **2005**, *110*. [CrossRef]
38. Edwards, C.S.; Bandfield, J.L.; Christensen, P.R.; Fergason, R.L. Global distribution of bedrock exposures on Mars using THEMIS high-resolution thermal inertia. *J. Geophys. Res. Planets* **2009**, *114*. [CrossRef]
39. Van de Griend, A.; Camillo, P.; Gurney, R. Discrimination of soil physical parameters, thermal inertia, and soil moisture from diurnal surf. *Water Resour. Res.* **1985**, *21*, 997–1009. [CrossRef]
40. Rosema, A.; Fiselier, J. Meteosat-based evapotranspiration and thermal inertia mapping for monitoring transgression in the Lake Chad region and Niger Delta. *Int. J. Remote Sens.* **1990**, *11*, 741–752. [CrossRef]
41. Cai, G.; Xue, Y.; Hu, Y.; Wang, Y.; Guo, J.; Luo, Y.; Wu, C.; Zhong, S.; Qi, S. Soil moisture retrieval from MODIS data in Northern China Plain using thermal inertia model. *Int. J. Remote Sens.* **2007**, *28*, 3567–3581. [CrossRef]
42. Matsushima, D.; Kimura, R.; Shinoda, M. A Study on Soil Moisture Estimation using Thermal Inertia. *J. Jpn. Soc. Civ. Eng. B1* **2012**, *67*. [CrossRef]
43. Cracknell, A.P.; Xue, Y. Estimation of ground heat flux using AVHRR data and an advanced thermal inertia model (SoA-TI model). *Int. J. Remote Sens.* **1996**, *17*, 637–642. [CrossRef]
44. Sobrino, J.A.; El Kharraz, M.H. Combining afternoon and morning NOAA satellites for thermal inertia estimation 1: Algorithm and its testing with Hydrologic Atmospheric Pilot Experiment-Sahel data. *J. Geophys. Res.* **1999**, *104*, 9445–9453. [CrossRef]
45. Sobrino, J.A.; El Kharraz, M.H. Combining afternoon and morning NOAA satellites for thermal inertia estimation 2. Methodology and application. *J. Geophys. Res.* **1999**, *104*, 9455–9465. [CrossRef]
46. Price, J.C. On the analysis of thermal infrared imagery: The limited utility of apparent thermal inertia. *Remote Sens. Environ.* **1985**, *18*, 59–73. [CrossRef]
47. Kahle, A.B. Surface emittance, temperature, and thermal inertia derived from Thermal Infrared Multispectral Scanner (TIMS) data for Death Valley, California. *Geophysics* **1987**, *52*, 858–874. [CrossRef]
48. Putzig, N.E.; Mellon, M.T. Apparent thermal inertia and the surface heterogeneity of Mars. *Icarus* **2007**, *191*, 68–94. [CrossRef]
49. Hildreth, W. Volcanological perspectives on Long Valley, Mammoth Mountain, and Mono Craters: Several contiguous but discrete systems. *J. Volcanol. Geotherm. Res.* **2004**, *136*, 169–198. [CrossRef]
50. Bailey, R.A. *Geologic Map of Long Valley Caldera, Mono-Inyo Craters Volcanic Chain, and Vicinity, Eastern California*; U.S. Geological Survey Map I-1933. U.S. Geological Survey: Reston, VA, USA, 1989.
51. Bursik, M.; Sieh, K. Range front faulting and volcanism in the Mono Basin, Eastern California. *J. Geophys. Res.* **1989**, *94*, 15587–15609. [CrossRef]

52. Wood, S. *Chronology of Late Pleistocene and Holocene Volcanics, Long Valley and Mono Basin Geothermal Areas, Eastern California*; United States Geological Survey Open File Report. U.S. Geological Survey: Reston, VA, USA, 1983.
53. Bailey, R.A. Quaternary volcanism of Long Valley Caldera and Mono-Inyo Craters, Eastern California. In *Field Trip Guidebook T313*; American Geophysical Union: Washington, DC, USA, 1989.
54. Sieh, K.; Bursik, M. Most recent eruption of the Mono Craters, Eastern Central California. *J. Geophys. Res.* **1986**, *91*, 12539–12571. [CrossRef]
55. Hill, D.P. *Response Plan for Volcano Hazards in the Long Valley Caldera and Mono Craters Region, California*; U.S. Geological Survey: Reston, VA, USA, 2002; Volume 2185.
56. Crumpler, L.S.; Aubele, J.C. Structural evolution of Arsia Mons, Pavonis Mons, and Ascraeus Mons: Tharsis region of Mars. *Icarus* **1978**, *34*, 496–511. [CrossRef]
57. Crumpler, L.S.; Head, J.W.; Aubele, J.C. Calderas on Mars: Characteristics, structure and associated flank deformation. In *Volcano Instability on the Earth and Other Planets*; McGuire, W.J., Jones, A.P., Neuberg, J., Eds.; Geological Society Special Publication: London, UK, 1996; Volume 110, pp. 307–348.
58. Head, J.W.; Siebert, N.; Pratt, S.; Smith, D.; Zuber, M.; Solomon, S.; McGovern, P.J.; Garvin, J.B.; The MOLA Science Team. Characterization of major volcanic edifices on Mars using Mars Orbiter Laser Altimeter (MOLA) data. In Proceedings of the 29th Lunar and Planetary Science Conference, The Woodlands, TX, USA, 16–20 March 1998.
59. Head, J.W.; Siebert, N.; Pratt, S.; Smith, D.; Zuber, M.; Garvin, J.B.; McGovern, P.J.; The MOLA Science Team. Volcanic calderas on Mars: Initial views using Mars Orbiter Laser Altimeter (MOLA) data. In Proceedings of the 29th Lunar and Planetary Science Conference, The Woodlands, TX, USA, 16–20 March 1998.
60. Mouginis-Mark, P.J. Prodigious ash deposits near the summit of Arsia Mons volcano, Mars. *Geophys. Res. Lett.* **2002**, *29*. [CrossRef]
61. Scott, D.; Zimbelman, J. *Geologic Map of Arsia Mons Volcano, Mars*; U.S. Geological Survey: Reston, VA, USA, 1995.
62. Ramsey, M.S.; Crown, D.A. Mantled lava flow surfaces on Earth: Thermo-physical analogs for Martian volcanism? In Proceedings of the American Geophysical Union, Fall Meeting, San Francisco, CA, USA, 5–9 December 2011.
63. Scott, D. *Map Showing Lava Flows in the Southeast Part of the Phoenicis Lacus Quadrangle of Mars*; U.S. Geological Survey: Reston, VA, USA, 1981.
64. Scott, D.; Schaber, G.; Dial, A. *Map Showing Lava Flows in the Southwest Part of the Phoenicis Lacus Quadrangle of Mars*; U.S. Geological Survey: Reston, VA, USA, 1981.
65. Scott, D.; Schaber, G.; Horstman, K.; Dial, A.; Tanaka, K. *Map Showing Lava Flows in the Northwest Part of the Phoenicis Lacus Quadrangle of Mars*; U.S. Geological Survey: Reston, VA, USA, 1981.
66. Bleacher, J.E.; Greeley, R.; Williams, D.A.; Cave, S.R.; Neukum, G. Trends in effusive style at the Tharsis Montes, Mars, and implications for the development of the Tharsis province. *J. Geophys. Res.* **2007**, *112*. [CrossRef]
67. Garry, W.B.; Williams, D.A.; Bleacher, J.E.; Dapremont, A.M. Geologic mapping of Olympus Mons and Tharsis Montes, Mars. In Proceedings of the 46th Lunar and Planetary Science Conference, The Woodlands, TX, USA, 16–20 March 2015.
68. Russell, I.C. *Quaternary History of the Mono Valley, California*; U.S. Geological Survey Eighth Annual Report. U.S. Geological Survey: Reston, VA, USA, 1889; pp. 267–394.
69. National Climatic Data Center (NCDC). NOAA, n.d. Web. 24 March 2013.
70. Google Earth. 37°53′42.34″ N, 119°0′16.07″ W. Available online: https://www.google.com/earth/ (accessed on 15 November 2012).
71. Abrams, M. The Advanced Spaceborne Thermal Emission and Reflection Radiometer (ASTER): Data products for the high spatial resolution imager on NASA's Terra platform. *Int. J. Remote Sens.* **2000**, *21*, 847–859. [CrossRef]
72. Realmuto, V.J. Separating the effects of temperature and emissivity: Emissivity spectrum normalization. In Proceedings of the 2nd TIMS Workshop, Pasadena, CA, USA, 6 June 1990; Jet Propulsion Laboratory Publication: Pasadena, CA, USA, 1990; pp. 90–155.
73. Ramsey, M.S.; Fink, J.H. Estimating lava vesicularity: A new technique using thermal infrared remote sensing data. *Am. Geophys. Union Eos Trans.* **1996**, *77*, F803.

74. Mars, J.C.; Rowan, L.C. Spectral assessment of new ASTER SWIR surface reflectance data products for spectroscopic mapping of rocks and minerals. *Remote Sens. Environ.* **2010**, *114*, 2011–2025. [CrossRef]
75. Lee, R.J.; King, P.L.; Ramsey, M.S. Spectral analysis of synthetic quartzofeldspathic glasses using laboratory thermal infrared spectroscopic methods. *J. Geophys. Res.* **2010**, *115*. [CrossRef]
76. Simurda, C.M.; Ramsey, M.S. Correcting topographic shadowing errors in apparent thermal inertia images. In Proceedings of the 45th Lunar and Planetary Science Conference, The Woodlands, TX, USA, 17–21 March 2014.
77. Anderson, S.W.; Stofan, E.R.; Plaut, J.J.; Crown, D.A. Block size distributions on silicic lava flow surfaces: Implications for emplacement conditions. *Geol. Soc. Am. Bull.* **1998**, *110*, 1258–1267. [CrossRef]
78. Vaughan, R.A., Ed.; *Remote Sensing Applications in Meteorology and Climatology*; Springer Science & Business Media: Berlin, Germany, 1987; Volume 201.
79. Mellon, M.T.; Jakosky, B.M.; Kieffer, H.H.; Christensen, P.R. High-resolution thermal inertia mapping from the Mars global surveyor thermal emission spectrometer. *Icarus* **2000**, *148*, 437–455. [CrossRef]
80. Ruff, S.W.; Christensen, P.R.; Barbera, P.W.; Anderson, D.L. Quantitative thermal emission spectroscopy of minerals: A laboratory technique for measurement and calibration. *J. Geophys. Res.* **1997**, *102*, 14899–14913. [CrossRef]

© 2016 by the authors; licensee MDPI, Basel, Switzerland. This article is an open access article distributed under the terms and conditions of the Creative Commons by Attribution (CC-BY) license (http://creativecommons.org/licenses/by/4.0/).